

Quantum control of nitrogen-vacancy
centers in diamond

**QUANTUM CONTROL OF NITROGEN-VACANCY CENTERS IN
DIAMOND**

A Thesis

Submitted to the Faculty

in partial fulfillment of the requirements for the

degree of

Bachelor of Arts

in

Engineering Sciences

by

Katherine Lasonde

DARTMOUTH COLLEGE

Hanover, New Hampshire

June 4, 2023

Examining Committee:

Douglas Van Citters, Chair

Eric Fossum

Chandrasekhar Ramanathan

Abstract

This thesis describes the construction and evaluation of an optically-detected magnetic resonance (ODMR) spectrometer for the purpose of quantum control of nitrogen-vacancy (NV) centers in diamond. This spectrometer operates in a low magnetic field and at ambient temperatures, and it only requires commercially available components. The current techniques used to initialize, control, and read out the state of nitrogen-vacancy centers, especially in the context of being a qubit sensor, are also reviewed. Applications of NV center spectrometer sensing includes the detection and imaging of single-neuron action potentials, single protein detection through nanoscale MRIs, investigations of meteorite composition and properties, as well as quantum computing and information.

Acknowledgements

First and foremost, I am deeply grateful to my advisors, Professors Chandrasekhar Ramanathan and Eric Fossum, for their unwavering guidance, encouragement, and invaluable insights. I would like to express my gratitude to my lab mates, Nicholas Shade, Henry Prestegaard, Tunmay Gerg, and Melody Tsutsumi Cruz, for their camaraderie and invaluable assistance throughout the project. Their genuine interest, enthusiasm, and support gave me the motivation and determination to persist in this research. Thank you to every friend and family member. I am eternally grateful for your belief in me and my work.

Finally, I am immensely thankful for the Stamps Foundation for their financial support during my off-term and early research period, as well as the Kaminsky Family Fund for their generous thesis award. This award enabled me to purchase a new diamond sample, which was essential for my research.

Contents

| | |
|--|-----------|
| Abstract | iii |
| Preface | iv |
| 1 Introduction | 1 |
| 1.1 Motivation for Quantum Technology | 1 |
| 1.2 Motivation for Studying NV Centers | 3 |
| 1.3 Extended Statement of Thesis | 3 |
| 2 Nitrogen vacancy centers in diamond | 7 |
| 2.1 Description at the atomic level | 7 |
| 2.2 Energy Levels | 9 |
| 2.3 Optical Manipulation of NV Centers | 11 |
| 2.3.1 NV Center sample information | 13 |
| 3 CW Experimental Setup | 14 |
| 3.1 Constructing a Tabletop Spectrometer | 14 |
| 3.2 Description of the setup | 15 |
| 3.2.1 Laser and ND Filter | 16 |
| 3.2.2 Mirrors and Collimators | 17 |

| | | |
|----------|---|-----------|
| 3.2.3 | Optical filtering and excitation | 19 |
| 3.2.4 | Read out via Image Sensor | 21 |
| 3.3 | Optically detected magnetic resonance spectra | 22 |
| 3.3.1 | ODMR Experimental Protocol | 22 |
| 3.3.2 | ODMR Experimental Results and Analysis | 23 |
| 3.4 | T_1 Decay Measurement | 25 |
| 3.4.1 | T_1 Experimental Setup | 25 |
| 3.4.2 | T_1 experimental results | 26 |
| 3.4.3 | T_1 experimental protocol | 29 |
| 3.4.4 | T_1 experimental results | 30 |
| 3.4.5 | T_1 Experimental Analysis | 32 |
| 4 | Control protocols | 35 |
| 4.1 | Microwave manipulation of an NV center | 35 |
| 4.2 | Pulsed ODMR spectra | 37 |
| 4.2.1 | Pulsed ODMR experimental setup | 37 |
| 4.2.2 | Pulsed ODMR experimental procedure | 38 |
| 4.2.3 | Pulsed ODMR Experimental Results | 40 |
| 4.2.4 | Pulsed ODMR experimental analysis | 41 |
| 4.3 | Rabi Oscillation Measurement | 42 |
| 4.3.1 | Rabi oscillation experimental setup | 42 |
| 4.3.2 | Rabi oscillation experimental results | 44 |
| 4.3.3 | Rabi Oscillation Experimental Analysis | 45 |
| 4.3.4 | Analysis of π and $\pi/2$ pulses | 46 |
| 4.4 | Hahn Echo (T_2 decay) measurement | 46 |

| | | |
|-----------------|--|-----------|
| 4.4.1 | Hahn Echo (T_2 decay) Experimental Setup | 46 |
| 4.4.2 | Hahn Echo (T_2 decay) Experimental Results | 48 |
| 4.4.3 | T_2 Experimental Analysis | 50 |
| 5 | The QIS vs. CMOS Analysis | 51 |
| 5.0.1 | Overview of Image Sensors | 51 |
| 5.0.2 | T_1 and T_2 experimental data collected via the photodiode . . | 53 |
| 5.0.3 | Calculations | 56 |
| 5.0.4 | Analysis | 57 |
| 5.0.5 | Conclusions and Recommendations | 58 |
| 6 | Conclusion | 61 |
| 6.1 | Future Research | 61 |
| 6.2 | Closing Remarks | 62 |
| Appendix | | 63 |
| 6.3 | Setup procedures | 63 |
| 6.3.1 | Version 3 - pulsed ODMR, Rabi oscillations, and Hahn Echo . | 63 |
| 6.3.2 | Quanta Image Sensor Setup | 64 |
| 6.3.3 | CMOS Image Sensor (Photodiode) Setup | 64 |
| 6.4 | Experiment Code | 64 |
| 6.4.1 | CW ODMR experiment code | 64 |
| 6.4.2 | T_1 decay experiment code | 65 |
| 6.4.3 | Pulsed ODMR experiment code | 73 |
| 6.4.4 | Rabi oscillation experiment code | 76 |
| 6.4.5 | Hahn Echo (T_2) experiment code | 79 |

| | | |
|-------|---------------------|----|
| 6.4.6 | QIS data collection | 81 |
| 6.5 | List of parts | 83 |
| 6.5.1 | Optical components | 83 |

Chapter 1

Introduction

1.1 Motivation for Quantum Technology

Quantum mechanics is the fundamental theory of physics that explains the behavior of matter and energy at the smallest scales. This theory has given rise to phenomena such as superposition, entanglement, and quantum tunneling, which are foundational to the evolution of cutting-edge quantum technologies. The following are significant technologies that utilize the principles of quantum mechanics:

1. **Quantum Computing:** Quantum computers utilize quantum bits, or qubits, instead of classical bits to perform computations. Qubits have the unique ability to exist in a superposition of states, which allows quantum computers to process information exponentially faster than classical computers for specific types of problems. This has the potential to revolutionize fields such as cryptography, numerical optimization, drug discovery, and artificial intelligence.
2. **Quantum Communication:** Quantum communication utilizes the principles

1.1 Motivation for Quantum Technology

of quantum entanglement and superposition to transmit information securely. For instance, quantum key distribution is a prominent method that enables two parties to create a shared secret key that is secure from eavesdropping due to the principles of quantum mechanics.

3. **Quantum Sensing:** Quantum sensors utilize the unique properties of quantum systems to achieve highly accurate measurements. Examples include atomic clocks, which utilize the oscillations of atoms to measure time with exceptional accuracy, and quantum magnetometers, which can detect minuscule changes in magnetic fields for applications such as brain imaging [23]. Other physical quantities, such as electric field strength, pressure, and temperature, can also be measured [22].

The focus of this thesis is on nitrogen-vacancy (NV) centers in diamond, which have significant potential in the fields of quantum sensing and quantum computing. Quantum sensing has the potential to offer unparalleled levels of precision and accuracy, especially in the field of biology and its related disciplines. Quantum sensors have the potential to enhance the sensitivity and resolution of current magnetic resonance imaging (MRI) techniques, including nanoscale MRIs (nanoMRI) [10]. Quantum sensors have the potential to enhance the imaging of biological tissues and detect smaller biomolecules, thereby improving diagnostics and understanding of various diseases. Similarly, quantum sensors have the potential to detect the presence of individual molecules, such as proteins, enzymes, and DNA, as well as their unique characteristics [10].

1.2 Motivation for Studying NV Centers

1.2 Motivation for Studying NV Centers

Nitrogen-vacancy centers in diamonds are highly promising candidates for quantum sensing due to their unique quantum and optical properties. Compared to other electronic spin defects, NV centers exhibit longer coherence times at room temperature. The coherence time characterizes the duration for which a quantum system can maintain its superposition state. In addition, NV centers can be optically initialized and read out, allowing for non-invasive detection of single-spin sensitivity. For example, NV centers can serve as magnetometers, conducting nanoMRIS within living cells by detecting the magnetic field produced by free radicals [13]. They are also among the few emerging quantum sensors that can be implemented in ambient conditions without requiring cryogenic temperatures. Consequently, it is possible to construct a spectrometer for controlling NV centers at low magnetic and ambient fields using commercially available components. The relatively simple design of the set-up enables undergraduate students to investigate the NV center as a quantum sensor.

1.3 Extended Statement of Thesis

This thesis explores the feasibility of conducting quantum control experiments at room temperature using a cost-effective tabletop spectrometer that employs nitrogen-vacancy (NV) centers. First, the theory behind the distinctive quantum and optical properties of NV centers will be discussed. An explanation of the building process will follow, demonstrating how to utilize the aforementioned quantum and optical properties of the NV center. A series of experimental protocols, as well as enhancements

1.3 Extended Statement of Thesis

to the experimental setup design, will be described. Below is a brief summary of the quantum experimental protocols that will be explained in detail in the following chapters.

| | CW ODMR | T_1 relaxometry | Pulsed ODMR | Rabi oscillations | Hahn Echo (T_2) |
|-----------|---------|-------------------|-------------|-------------------|---------------------|
| Laser | | | | | |
| Microwave | | None | | | |
| Readout | | | | | |

Figure 1.1: Summary of NV center key experimental differences. Figure adapted from Levine et. al [9].

1. **Continuous Wave (CW) ODMR:** This technique is used to investigate the magnetic resonance properties of NV centers. By optically detecting changes in fluorescence in response to an applied microwave frequency, we can accurately determine the resonance frequency of the NV center. The resonance frequency is a crucial piece of information when attempting to manipulate the state of NV centers. It will be explored at the beginning of Chapter 3 and from the middle to the end of Chapter 4.
2. **T_1 Relaxometry:** This experiment measures the relaxation time (T_1) of the electron spin of the NV center. T_1 is the time required for the electron spin to return to its equilibrium state after being excited. By studying the T_1 decay, we

1.3 Extended Statement of Thesis

can gain insight into the maximum duration for which quantum coherence can be sustained in an NV center. This experiment will be conducted and analyzed at the end of Chapter 3.

3. **Pulsed ODMR:** Pulsed ODMR is a technique used to study the magnetic resonance properties of NV centers, similar to CW ODMR. However, instead of applying continuous microwave excitation, pulsed ODMR utilizes short microwave pulses. This method provides improved spectral resolution and sensitivity, allowing for more precise measurement of the resonance frequencies of electron spin transitions in the NV center. An overview of this experiment is included at the beginning of Chapter 4.
4. **Rabi Oscillation:** The Rabi oscillation protocol involves the coherent manipulation of the electron spin of the NV center using microwave pulses. By analyzing the time evolution of the emitted fluorescence, it is possible to determine the microwave pulse lengths required to rotate an NV center by 90 degrees ($\pi/2$ radians) or 180 degrees (π radians). Another decay constant value, known as T_2^{Rabi} , can be measured. The details of the Rabi oscillation protocol are included in the middle of Chapter 4.
5. **Hahn Echo:** The Hahn Echo protocol is performed to measure the coherence time (T_2) of the electron spin of the NV center. T_2 is the duration during which the electron spin remains coherent before being influenced by its environment. Similarly, measuring the T_2 value helps improve understanding of the time limit of quantum coherence in an NV center. This experiment, which is described in Chapter 4, will be the final one presented in the thesis.

1.3 Extended Statement of Thesis

In summary, these experiments are essential for characterizing and understanding the properties of NV centers in diamond. The data obtained from these experiments can be utilized to enhance the performance of NV centers for diverse applications and offer valuable insights into the fundamental physics of these fascinating quantum systems. The theory, setup, and results of each experiment will be explained in further detail in the following chapters.

Chapter 2

Nitrogen vacancy centers in diamond

2.1 Description at the atomic level

Diamond is a semiconductor with a wide bandgap of 5.4 eV. Point defects in the lattice introduce unpaired electron spins. The most abundant impurity found in diamonds is nitrogen, as noted by Popa in a study on pulsed magnetic resonance [16]. This is a substitutional defect in which a nitrogen atom replaces a carbon atom in the crystal lattice. To create a nitrogen-vacancy center in diamond, two adjacent carbon atoms are replaced by a single nitrogen atom. This creates a vacancy or hole in the lattice structure due to the absence of an atom [5]. Since the vacancy has no associated electrons, the three adjacent carbons, which were previously covalently bonded to the removed carbon, are now left unpaired. To increase stability, the unpaired electrons of the two adjacent carbon atoms form a quasi-covalent bond (highlighted in pink in Figure 2.1). The center carbon atom then oscillates between forming covalent bonds

2.1 Description at the atomic level

with the adjacent carbon atoms on its left and right [5]. Finally, the three unpaired electrons remaining in the NV center form a triplet spin state, which is a fundamental aspect of the quantum model.

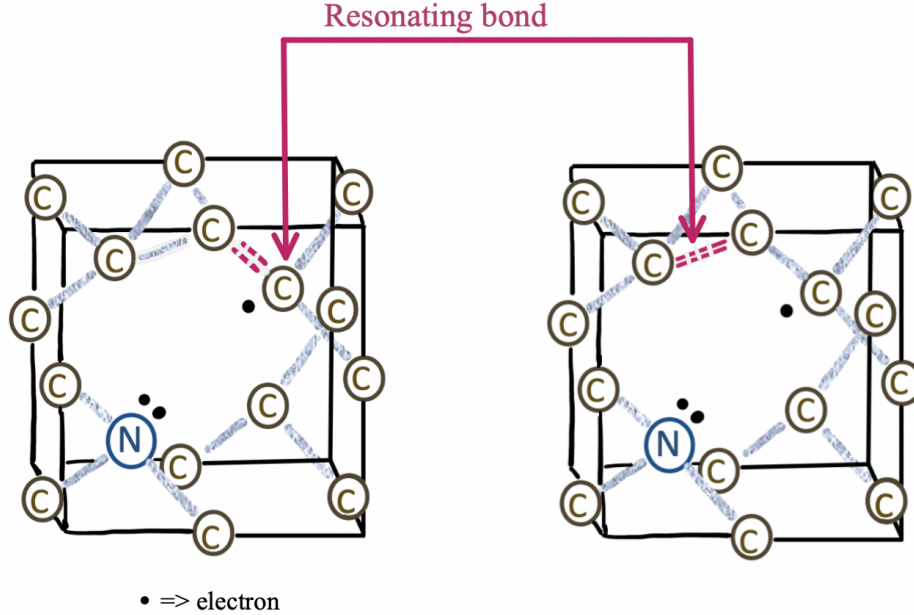


Figure 2.1: Atomic structure of a diamond lattice. The black dots represent unpaired electrons, while the brown circles labeled with a "C" denote carbon atoms. The blue circle labeled with an "N" represents a nitrogen atom. The pink double bond is the resonant bond.

There are two naturally occurring charge states for NV centers in diamond: neutral (NV_0) and negative (NV^-). Although the ground state configuration of the NV center is more common, it is possible to convert NV_0 to NV^- by applying an external voltage [3]. The NV^- center is more advantageous for quantum technologies than the NV_0 center because it has a significantly longer coherence time [3]. The presence of an additional electron in the NV^- configuration enhances the stability of the quantum mechanical system and mitigates the impact of external noise and perturbations

2.2 Energy Levels

through a phenomenon called electron shielding [7]. For the remainder of this paper, any reference to an NV center will pertain to the NV^- state, unless stated otherwise.

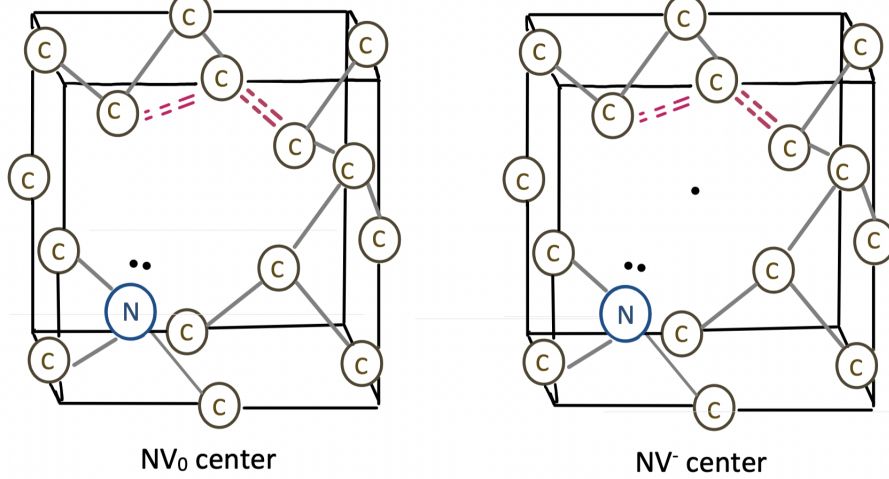


Figure 2.2: Atomic level diagram of the NV_0 center (left) vs. the NV^- center (right), which are the two most common charge states of NV centers. The NV^- center has three unpaired electrons, whereas the NV_0 center has only two. Symbols are identical to those depicted in Figure 2.1.

2.2 Energy Levels

NV center triplets have an electronic ground state and excited states titled the 3A_2 and E_3 states, respectively. These two states are separated by 1.95 eV [10]. According to Misonou, a photon with a wavelength of approximately 620-625 nm provides the optimal amount of energy required to excite an electron from the ground state to the first excited state [10].

Since NV center electrons emit red photons with a wavelength of 637 nm, it is more convenient to excite the NV center using green photons. This allows for the use of filtering to accurately identify whether a photon is from the exciting laser or is emitted

2.2 Energy Levels

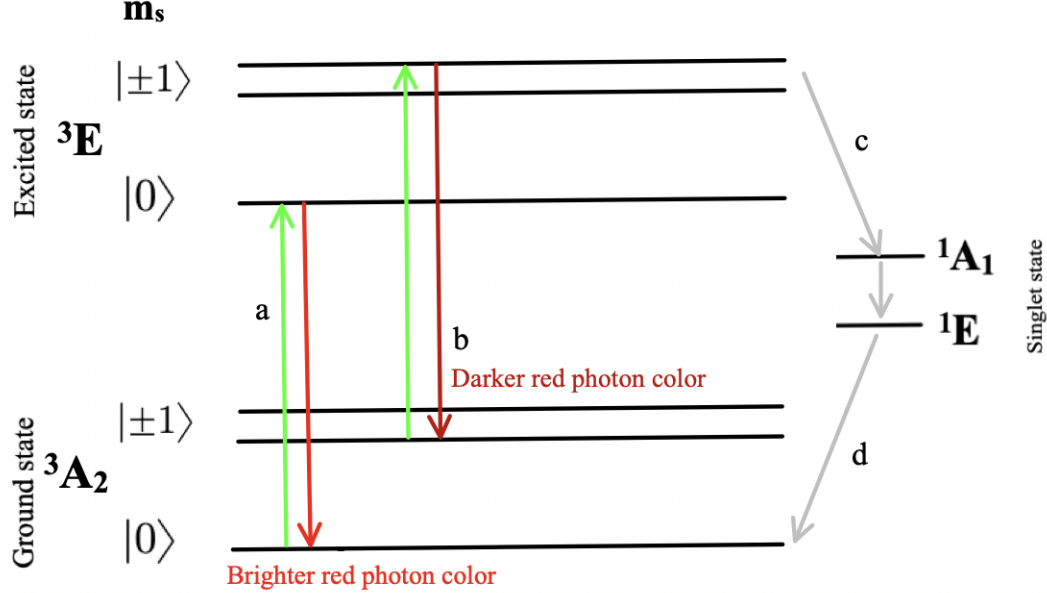


Figure 2.3: Energy diagram of an NV center: a. Green laser excitation (spin-preserving) b. Radiative decay (spin preserving) c. Decay to singlet state (spin dependent) d. Non radiative decay

from the NV center. Thus, as is conventional in NV center experimental protocols, a green laser was used throughout the experiment. The energy level diagram depicted in Figure 2.3 illustrates the triplet ground state, the triplet excited state, and a singlet metastable state [16]. Both the ground state and the first excited state of the NV center are located within the energy band gap.

When a green laser is directed onto an NV center, it provides approximately 2.4 eV of energy, which excites the unpaired electrons from the ground state to the excited 3E state [10]. The electrons can then relax back to the ground state through either radiative or non-radiative pathways. The process of radiative relaxation involves the emission of a red photon. Around 0.4 eV is lost due to the vibrational motion of

2.3 Optical Manipulation of NV Centers

the NV center, resulting in the emitted photon having less energy and a shorter wavelength than the absorbed photons. [23]. However, non-radiative relaxation via the singlet state, as shown in Figure 2.3 by the gray arrows, does not result in the emission of a red photon.

The process of an electron decaying radiatively or non-radiatively depends on its initial spin state, as will be explained in the following subsection. Electrons in the $m_s = \pm 1$ sub-level have a higher probability of non-radiative relaxation, while electrons in the $m_s = 0$ sub-level are more likely to undergo radiative relaxation, resulting in the emission of a photon. Therefore, the intensity of photoluminescence corresponds directly to the spin state of the NV center. As a result, the quantum state of the NV center can be determined by analyzing the intensity of the emitted photons [9]. Specifically, an NV center appears to emit approximately 30% more photons when decaying from the $|0\rangle^3 E$ state compared to the $|\pm 1\rangle^3 E$ state [19]. Thus, to summarize, the $m_s = 0$ spin state of the NV center appears significantly brighter than the $m_s = \pm 1$ spin state.

2.3 Optical Manipulation of NV Centers

The NV center triplet is a spin-1 system with three states: $m_s = -1, 0$, and $+1$ [8]. The triplet sublevel exhibits a phenomenon known as zero-field splitting, which refers to the separation of energy sublevels within a triplet state, even in the absence of an external magnetic field. In this case, the $m_s = 0$ and $m_s = \pm 1$ sublevels of the NV center undergo splitting as a result of dipole-dipole coupling between electron spins [16]. Thus, the $|\pm 1\rangle$ states in an NV center are separated from the $|0\rangle$ state by an energy of $E = h\nu$, where $h = 6.62 \times 10^{-34} (\text{m}^2 \cdot \text{kg})/\text{s}$ and $\nu = 2.87 \text{ GHz}$ [8]. The

2.3 Optical Manipulation of NV Centers

$|+1\rangle$ and $| -1\rangle$ states are still degenerate, however.

Furthermore, the ratio of spins in each state can be determined using the Boltzmann factor, which is proportional to $e^{-\Delta E/k_b T}$. Here, ΔE represents the difference in energy of the states in Joules, while the Boltzmann constant is denoted by $k_B = 1.38 \times 10^{-23}$ J/K, and T represents the absolute temperature in Kelvin. Since the energy of the state is much less than the product of Boltzmann's constant and temperature, we can approximate $e^{-\Delta E/k_b T}$ as e^0 , which is approximately equal to 1. Thus, since the Boltzmann factor is proportional to a constant value (e.g., 1), the ratio of state populations is nearly equal [4].

When a green laser is directed onto an NV center, the spins of the NV center begin to constantly cycle continuously between the ground and excited states. Since the spins in the $|\pm 1\rangle$ state can decay through the singlet state to the $|0\rangle$ state, while the reverse process is forbidden, it is highly probable that after a sufficiently long period of time (≥ 3 μ s), all spins will eventually be initialized into the $|0\rangle$ state. Therefore, when a green laser is shone onto an NV center for ≥ 3 μ s, it initializes the state of the NV center to $|0\rangle$.

When the laser is turned off, however, the spins will no longer have enough energy for continuous cycling, and they will return to their ground state. It is in this moment that the number of emitted photons can be measured to determine the spin state of the quantum system, with a brighter read out denoting the $|0\rangle$ state and a darker read out denoting the $|\pm 1\rangle$ state. To distinguish between the transitions $|0\rangle \longleftrightarrow | -1\rangle$ and $|0\rangle \longleftrightarrow | +1\rangle$, a weak magnetic field can be applied to remove the degeneracy of the energy levels. The two states will resonate in slightly different microwave fields.

2.3 Optical Manipulation of NV Centers

2.3.1 NV Center sample information

The diamond sample used in this thesis is a high-quality CVD diamond crystal that was purchased from Element Six, a leading global producer of synthetic diamonds [23]. The sample was grown to dimensions of 3 mm x 3 mm x 300 μm with the aim of achieving a high concentration of 1 ppm nitrogen impurities. To create vacancies, the diamond sample was subjected to electron irradiation, receiving a dose of $2 \times 10^{18} \text{ cm}^{-2}$ on each side, resulting in a total dose of $4 \times 10^{18} \text{ cm}^{-2}$. This process strategically displaces carbon atoms from their lattice positions, creating vacancies in the crystal structure.

After the irradiation process, the sample underwent a 2-hour annealing period at a temperature of 800°C. This crucial step facilitated the migration of vacancies and their interactions to the site of the nitrogen atom. By carefully controlling the irradiation and annealing processes, it is possible to optimize the creation of NV centers in diamond. These centers have potential applications in quantum technologies. Depending on the concentration of defects in the diamond, the characteristics of its NV center will vary.

Chapter 3

CW Experimental Setup

3.1 Constructing a Tabletop Spectrometer

Before running quantum control protocols on a nitrogen-vacancy center, it is necessary to design and construct a device that can facilitate this process. Initial design planning was based on the papers by Misonou et al. [10] and Zhang et. al. [23]. The process of building the setup will be illustrated below through a series of pictures and explanations. Figure 3.1 shows a schematic of the initial configuration of the ODMR spectrometer and Figure 3.2 shows a photograph of the constructed system. The function of the different components is described below. Building the setup took up the majority of my research time, but the experiments conducted on it afterward validate the setup was constructed correctly. Thus, the thesis places more emphasis on the experiments than the construction.

3.2 Description of the setup

3.2 Description of the setup

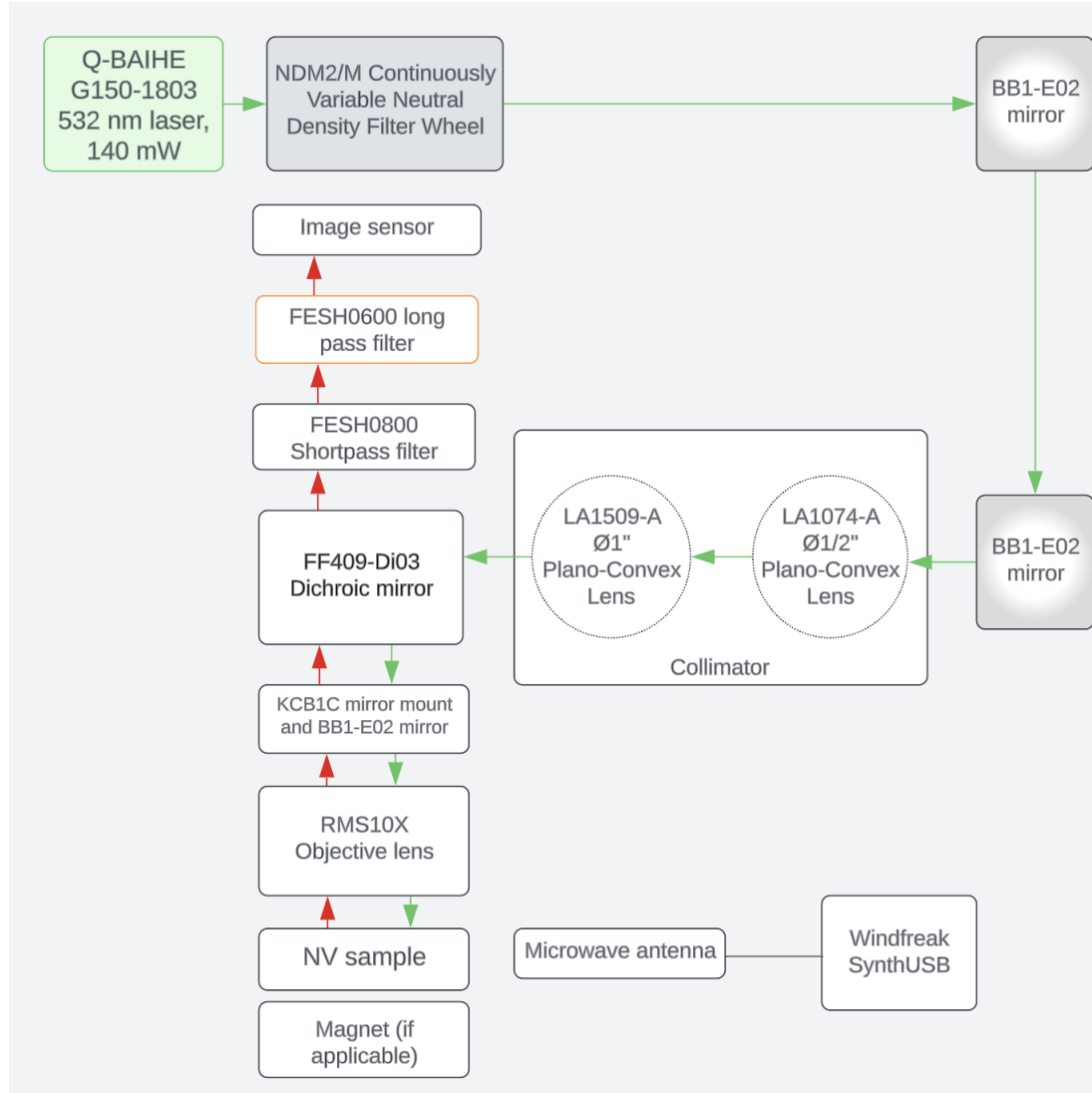


Figure 3.1: Schematic of version 1 of the experimental setup

3.2 Description of the setup

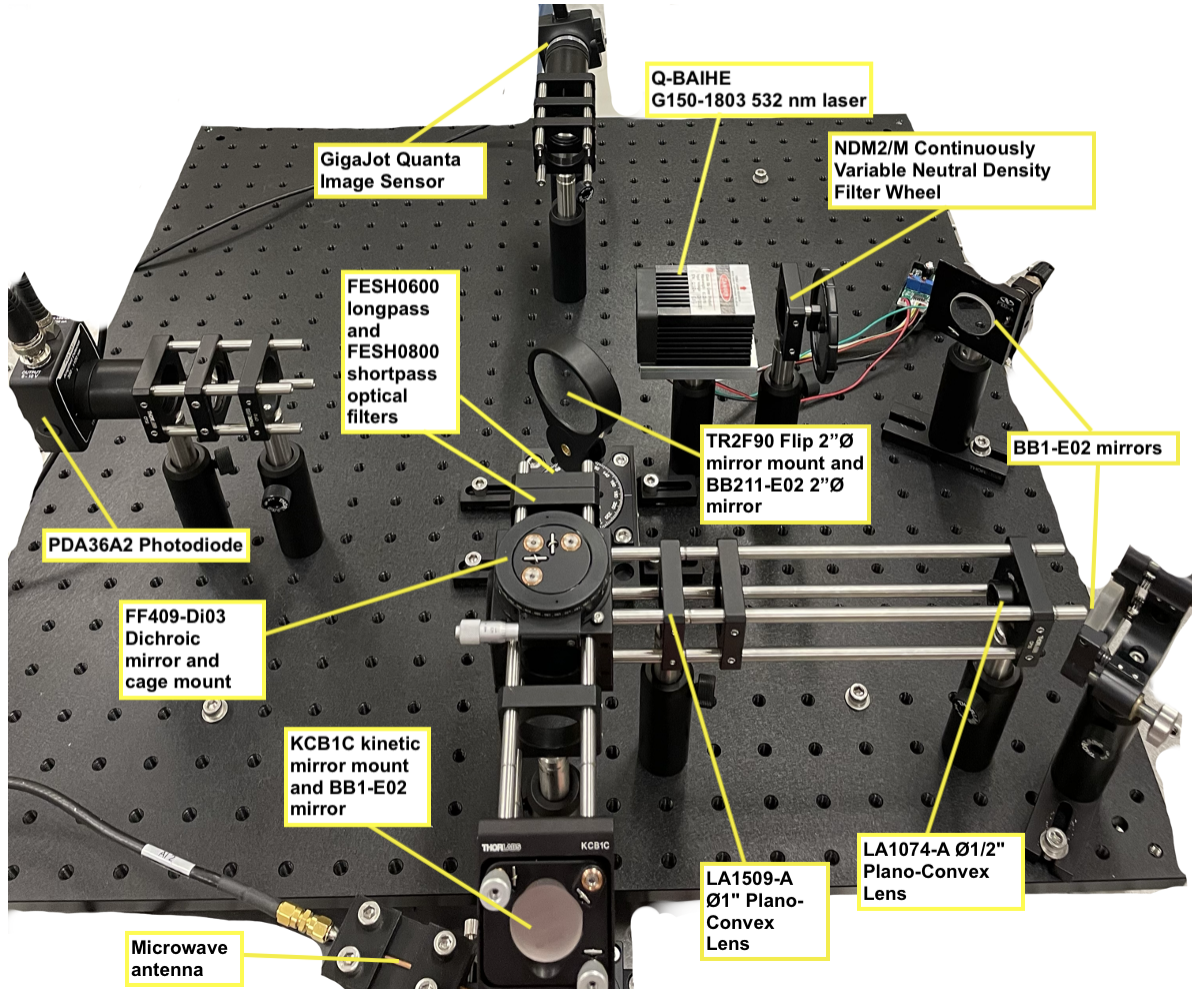


Figure 3.2: Image of version 1 of the experimental setup

3.2.1 Laser and ND Filter

The entire experimental setup is located in a semi-light tight box constructed of black cardboard. Initially, the Civil Laser G150-1803 (532 nm) green laser emits light which passes through a Thorlabs NDM2/M continuously variable neutral density (ND) filter wheel mounted to a cage system. The laser has an output power of 150 mW and a power size of 80mm x 46.1mm x 34mm (length x width x height). The

3.2 Description of the setup

ND filter is made of silica glass with a metallic coating that reduces the power level of the laser beam according to the angle of the filter. Specifically, the optical density of the ND filter is directly proportional to the angle of the filter, as described by the equation $OD = m * \theta$, where m is a constant value of 0.00741 for this particular filter. Everything after the laser is mounted onto a 30 mm x 30 mm cage system.

The laser utilized in this experiment is known as a Class 3B laser. This means that eye injury from the laser is possible. Before using a Class 3B laser, it is important to obtain a safety or training certificate. Additionally, it is imperative to use optical filtering glasses with a minimum of 2.0 optical density at 532 nm.

3.2.2 Mirrors and Collimators

Following the ND filter, the laser light is perfectly centered using Thorlabs BB01-E02 broad dielectric mirrors, angled by hand, to pass through a collimator. The collimator consists of two converging lenses that adjust the width of the laser beam. The first lens in the collimator is the Thorlabs LA1509-A Ø1" Plano-Convex Lens with a focal length f_1 equal to 100 mm. The second lens is the Thorlabs LA1074-A Ø1/2" Plano-Convex Lens with a focal length f_2 equal to 20 mm. Figure 3.3 shows a schematic of the collimator.

3.2 Description of the setup

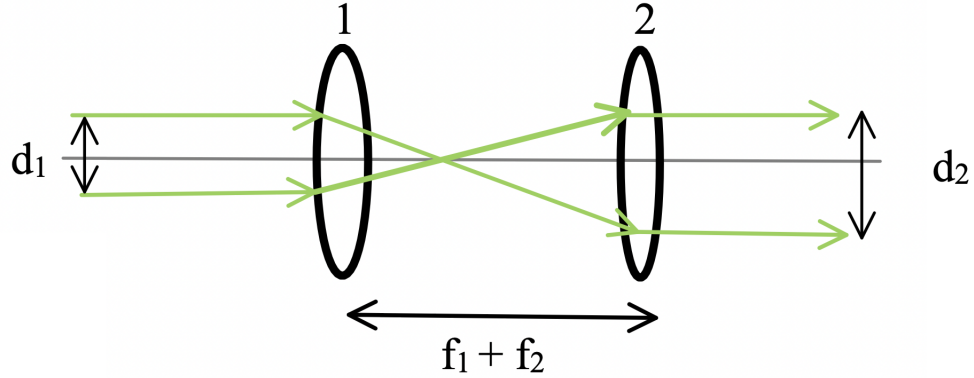


Figure 3.3: Collimator

The purpose of the collimator is to shape the laser beam into a well-defined, intense, and narrower beam. The precision of the collimator largely depends on the focal points of its two converging lenses. When the beam is focused on the focal point, photons that are not traveling in the intended direction will either be absorbed or scattered. Thus, only the desired photons will continue to the diamond sample. Furthermore, when the distance between two converging lenses is equal to the sum of their two focal lengths, parallel light entering from the right end will emerge parallel at the left end with a larger radius of curvature. This occurs because $f_2 = 20\text{mm} < f_1 = 100\text{mm}$. In the described setup, if the distance between the two lenses is 12 cm, the laser light is collimated. Ideally, the diameter of the collimated beam should be equal to the pupil diameter of the objective lens pupil diameter [10].

3.2 Description of the setup

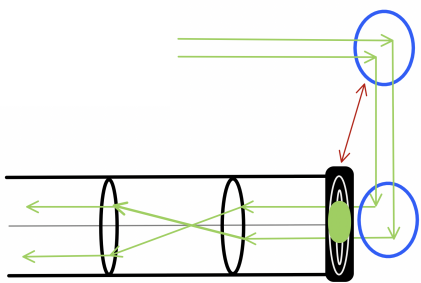


Figure 3.4: Optical alignment relationship between the first mirror and collimator

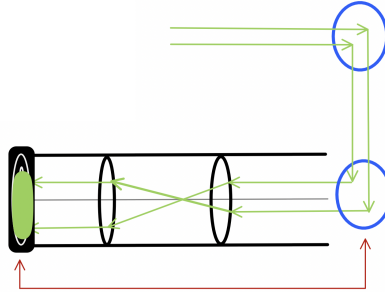


Figure 3.5: Optical alignment relationship between the second mirror and collimator

The laser path is then optically centered through the setup using two Thorlabs BB01-E02 mirrors. As shown in Figure 3.4, the first mirror's adjustments are used to center the laser beam at the beginning of the collimator cage. As shown in Figure 3.5, the angle of the second mirror is adjusted to center the beam at the end of the collimator cage. When aligning a beam through the collimator, it is crucial to repeat the adjustment process for both the first and second mirrors several times. This is because any changes in the angle of one mirror will impact how the beam reflects off the other. To check if the laser beam is collimated, the size of the beam should remain constant regardless of the distance after passing through the second lens.

3.2.3 Optical filtering and excitation

Once collimated, the laser beam passes through the Thorlabs FF409-Di03-25x36 shortpass dichroic mirror, which redirects the green laser light towards the NV diamond sample. The dichroic mirror utilized in this setup reflects green light and transmits red light. The filter is mounted to the cage system via the Thorlabs CM1-DCH cage cube for rectangular optics. A Thorlabs KCB1C right angle kinematic

3.2 Description of the setup

mirror and another Thorlabs BB01-E02 mirror are then used to direct the laser beam through an objective lens towards the diamond sample. A Thorlabs RMS10X objective lens is placed at a distance of 45.06 mm (the parafocal length) from the NV center sample. This objective lens is used to focus the green light intensely onto the diamond sample. The diamond samples is placed on an ToAUTO xyz axis manual linear stage to allow for position adjustment (up to 6.5 mm x 6.5 mm x 10 mm) of the sample without affecting the optical alignment of the setup. A small microwave antenna, positioned in the shape of a loop, is directly above the NV center which is held by a separate mount, moveable in both the polar coordinate z and ϕ directions. The loop located at the end of the microwave is designed to generate an oscillating magnetic field at the precise position of the diamond [19].

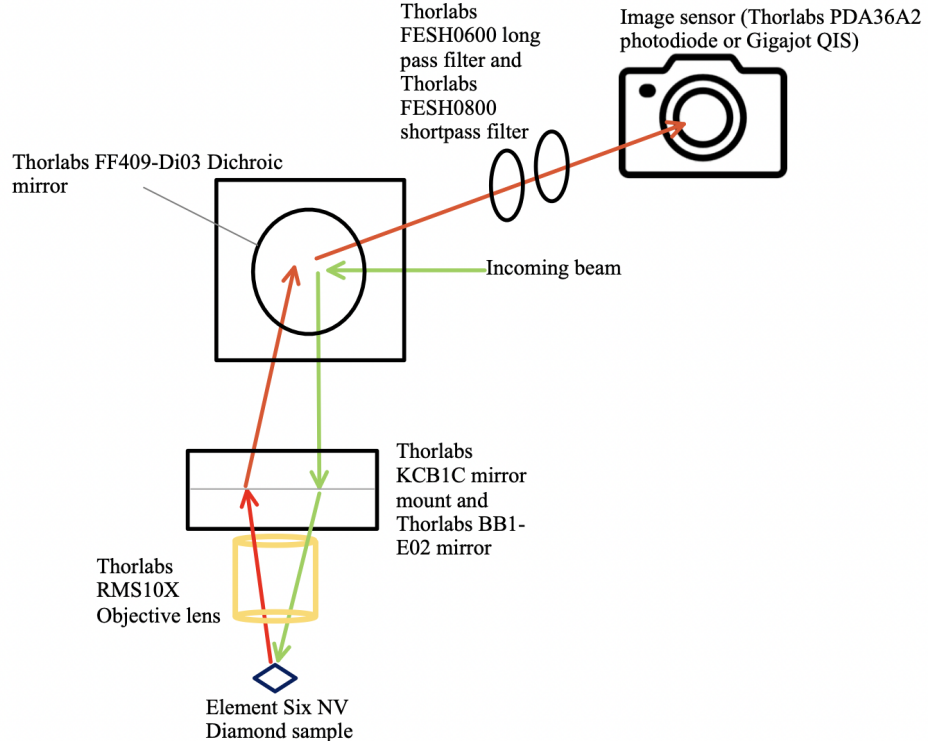


Figure 3.6: Dichroic filter side view

3.2 Description of the setup

Once the diamond sample absorbs the green photons from the laser beam, it emits a stream of red photons that are reflected back towards the objective lens. Because the diamond sample is positioned at the focal point of the objective, the red photons it emits also pass through the objective and emerge parallel to the green photon stream. The red light is able to pass through the dichroic mirror, while the green light is reflected. In the event that non-red photons pass through the dichroic filter, two additional optical filters are utilized: the Thorlabs FELH0600 longpass filter and the Thorlabs FESH0800 shortpass filter. Since red light has a wavelength of around 700 nanometers, it is able to pass through while green light, which has a wavelength of 532 nm, cannot.

3.2.4 Read out via Image Sensor

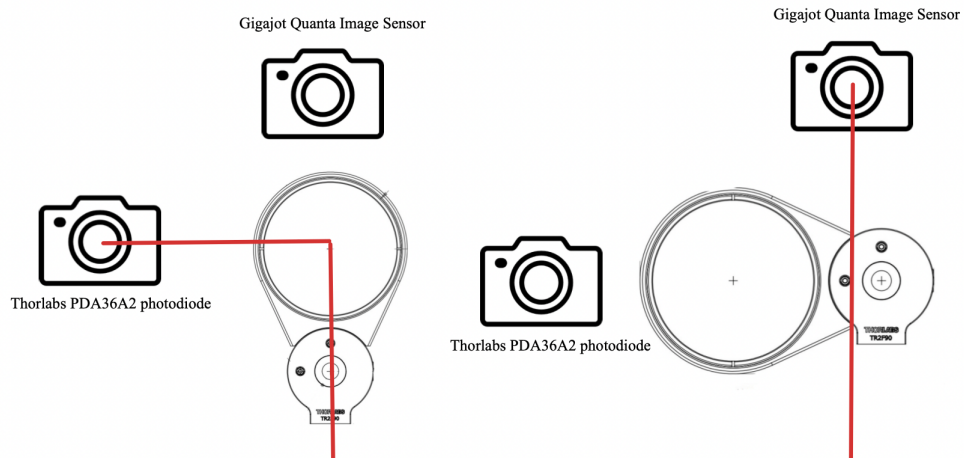


Figure 3.7: Flip mirror positions, 0° and 90°

After the optical filters, the Thorlabs TR2F90 90° Flip Mount with a Thorlabs PF20-03-G01 Ø2" Protected Aluminum mirror is used to direct the red light to the

3.3 Optically detected magnetic resonance spectra

photodiode or the QIS camera for read out, depending on whether it is angled at 0° or 90° . More specifications of the photodiode and QIS will be discussed in Chapter 5. As shown in 3.7, when the mirror is at 0° , emitted photons will be detected through the photodiode. When the mirror is angled at 90° , then emitted photons will be detected via the QIS. The differences between these two image sensors will be briefly discussed in the next paragraph, but the entirety of Chapter 7 is dedicated to this topic. To center the flip mirror over the upcoming red light, a slide mount was used. Furthermore, the photodiode utilized a Thorlabs LA1252-A plano-convex (with a focal point of 25.4 mm) to assist in converging the beam on the sensor. The QIS did not utilize a converging lens. Furthermore, although the QIS came with software for automatic data collection, the photodiode did not. Thus, the photodiode required connection to an oscilloscope called the Picoscope 2206B Oscilloscope with data collection software. The Picoscope has two input BNC connectors, one of which is connected to the output signal of the photodiode. Both the QIS software and the Picoscope software interface nicely with MATLAB. Finally, since the photodiode was much less sensitive to changes in the NV center, particularly at high speeds, a Stanford research systems model SR560 low-noise amplifier was used to amplify the photodiode signal before digitization with the Picoscope.

3.3 Optically detected magnetic resonance spectra

3.3.1 ODMR Experimental Protocol

In this protocol, the fluorescence emitted by the NV center is measured while the diamond is being excited by a continuous green laser and a microwave magnetic

3.3 Optically detected magnetic resonance spectra

field. The frequency of the microwaves are swept from 2825 MHz to 2920 MHz. The spin state of the NV center is influenced by the radio frequency (RF) field through a phenomenon known as electron spin resonance (ESR), which forms the basis of the ODMR technique [19]. The applied RF field can induce transitions between the $m_s = 0$ and $m_s = \pm 1$ levels of the NV center when it is resonant with these transitions. Monitoring the fluorescence emitted by the NV center while varying the RF frequency enables the characterization of the frequencies of energy transitions.

3.3.2 ODMR Experimental Results and Analysis

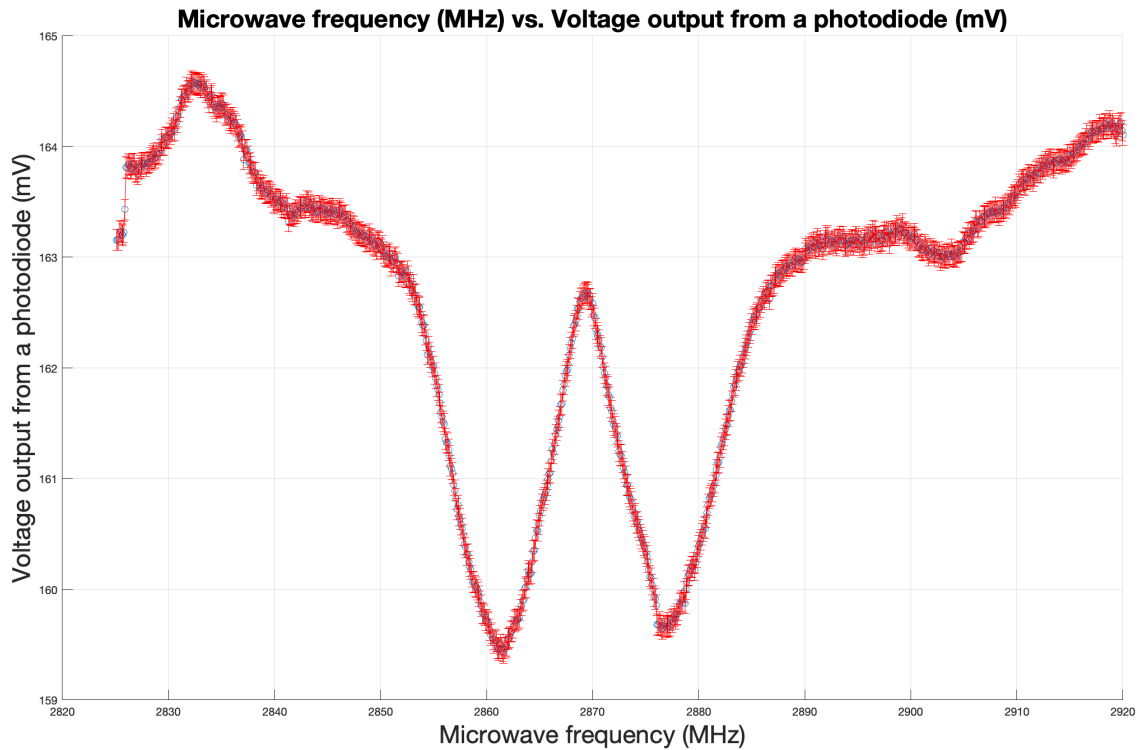


Figure 3.8: ODMR Spectra of an NV center recorded via the Thorlabs photodiode

3.3 Optically detected magnetic resonance spectra

The green laser remained on continuously as the frequency of the RF field was gradually swept from 2825 to 2920 MHz with a step size of 0.1 MHz. The Thorlabs PDA36A2 photodiode was used to capture and collect data in real-time, which was then recorded in an Excel spreadsheet. The standard deviation of the graph between 2890.6 MHz and 2900 MHz was calculated using the STDEV.S function in Excel, as this section of the graph is expected to be flat. Across the 2890.6-2900 MHz region, the standard deviation was found to be 0.906 mV. The assumption was made that the standard deviation of this portion of the data was representative of the entire data collection. Finally, a MATLAB script was used to generate Figure 3.9, which displays the scatter plot of ODMR frequency versus voltage, along with error bars sized according to the previously calculated standard deviation. (The MATLAB code for this and other experiments is attached in the appendix.)

While the laser initializes the spins to the $m_s = 0$ state, resonant microwaves can excite transitions to the $m_s = \pm 1$ states, which can decrease the fluorescence. Notably, the reason for two dips (rather than one) is due to the Zeeman effect. The presence of the Halbach magnet in this experiment lifts the degeneracy of the ± 1 states, separating them slightly. Thus, each dip in resonance is caused by distinct induced transitions between the $m_s = 0 \longleftrightarrow m_s = +1$ and $m_s = 0 \longleftrightarrow m_s = -1$ states, as explained earlier.

3.4 T_1 Decay Measurement

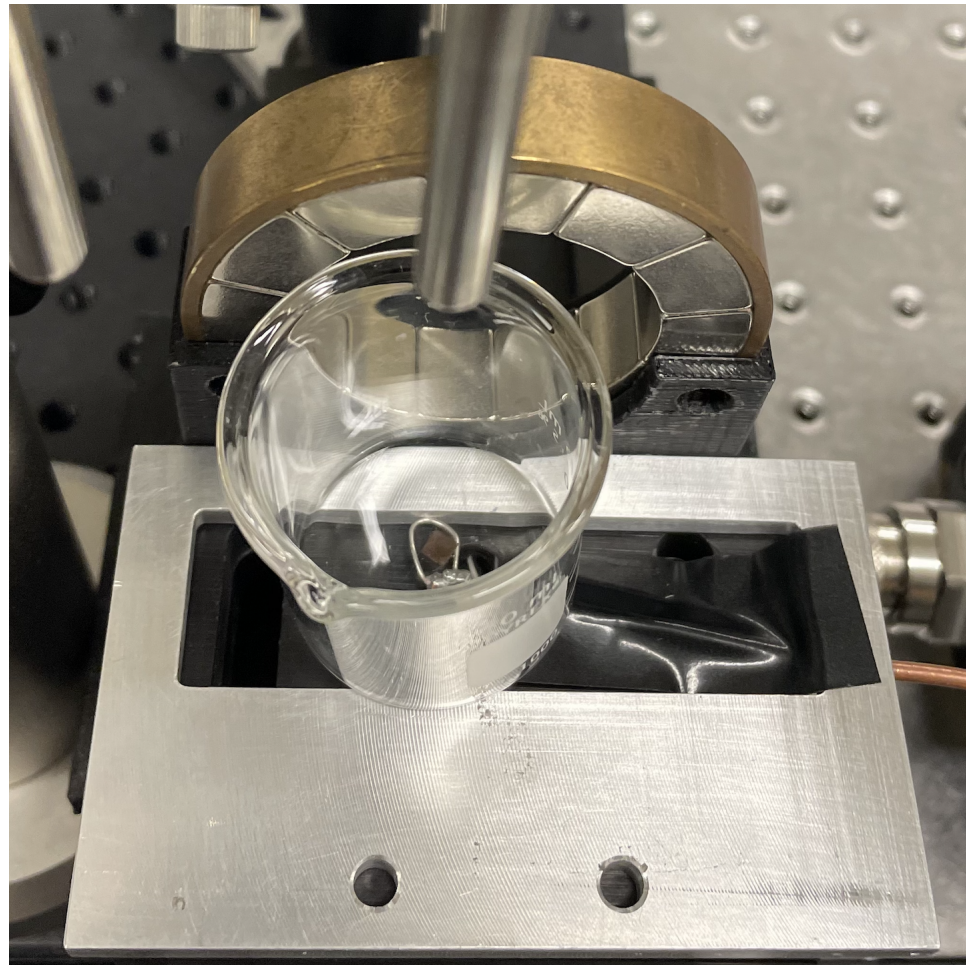


Figure 3.9: External Halbach magnet, NV sample, and microwave antenna. The Halbach magnet lifted the degeneracy between the $|+1\rangle$ and $| -1\rangle$ states, resulting in two dips in the spectra. In Chapter 4, a pulsed ODMR spectra without a magnet will show only one dip, as the $|+1\rangle$ and $| -1\rangle$ states are degenerate.

3.4 T_1 Decay Measurement

3.4.1 T_1 Experimental Setup

The T_1 measurement of an NV center relates to the time it takes for the electrons in an NV center to return to thermal equilibrium [10]. The T_1 experimental protocol

3.4 T₁ Decay Measurement

differs from the ODMR protocol in that the laser light is no longer continuous, but instead pulsed. In order to implement this, a SpinCore board, which is similar to an FPGA, was added to the setup. The SpinCore board features a MATLAB interface that enables pre-programming of TTL lines. To prevent degradation of TTL signals over time, a buffer box was constructed using the schematic provided in the user manuals for the SpinCore board. The final TTL buffer box was built by Jeffrey Renk, an electrician in the Dartmouth Physics Department.

3.4.2 T₁ experimental results

Although the laser in the setup could be directly turned on and off by a TTL line, the laser used in the experiment can only switch at a maximum rate of 30 kHz. The rate is too slow to implement most quantum control protocols for an NV center. Thus, the IntraAction Corp 802AF1 acousto-optic modulator (AOM), controlled by the TTL line, was used to modify the state of the laser.

An AOM is an electro-optic device that enables real-time manipulation of laser light through RF signals [17]. Depending on the RF signal, the AOM will either permit light to pass through or be blocked via a complex beam diffraction and deflection. Because of the deflection, the outputted beam has a separation angle. For this specific AOM, an 80 MHz RF signal with a drive power of 2 Watts is required to most effectively control whether laser signal is blocked or not. Furthermore, the beam separation angle for this AOM we have is 0.7 degrees. Thus, over a 200 mm distance, there is an expected deflection of about 2.6 mm between the main beam and the diffracted beam.

3.4 T₁ Decay Measurement

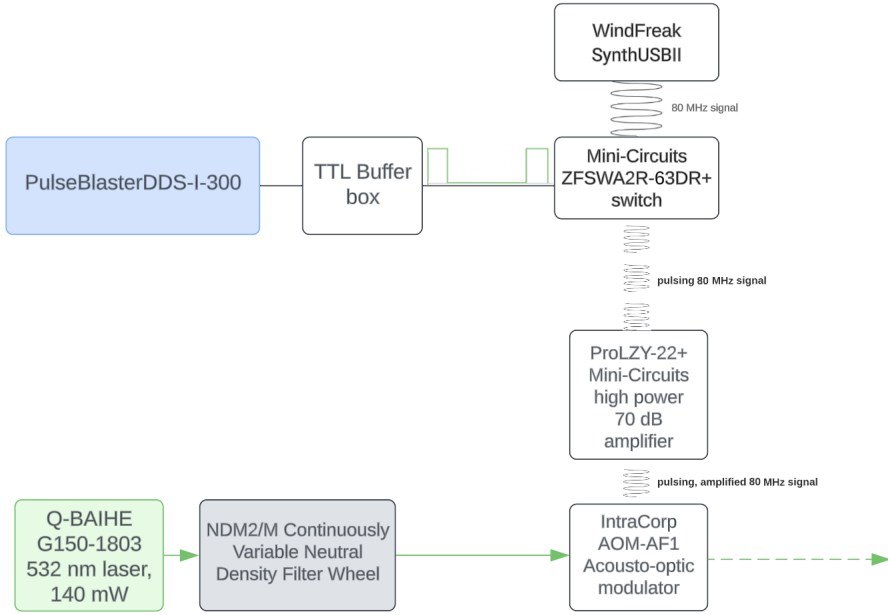


Figure 3.10: Detailed description of RF signal modification for the experiment.

In order to properly supply the required 80 MHz RF signal with 2 Watts of power, a WindFreak RF signal generator was interfaced to a Mini-Circuits ZASWA-2-50DRA+ switch. This switch would take in the TTL signals from the Pulseblaster, and then output an RF signal of the same frequency as the WindFreak in the timing sequence dictated by the Pulseblaster. This outputted RF signal was only 100 mV peak to peak however, and thus needed to be amplified to provide a signal with enough power to the AOM. Therefore, a Fairview Microwave 4 dB Fixed Attenuator and a LZY-22+ Mini-Circuits 70 dB high power amplifier were connected between the output of the switch and the input of the AOM, to amplify the signal by a net of 64 dB.

3.4 T₁ Decay Measurement

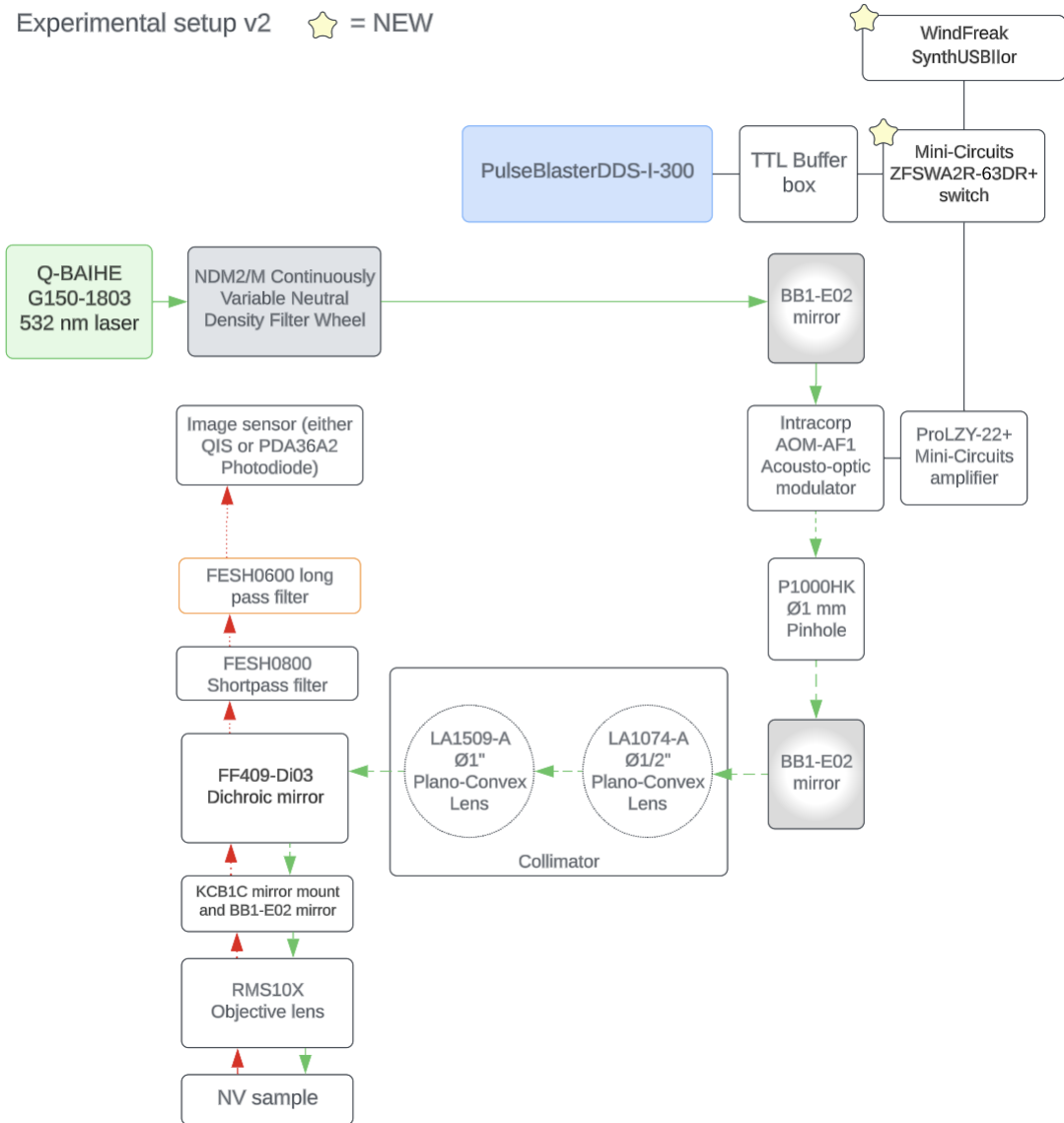


Figure 3.11: Second iteration of the experimental setup schematic, a star denotes an addition since the first version

3.4 T_1 Decay Measurement

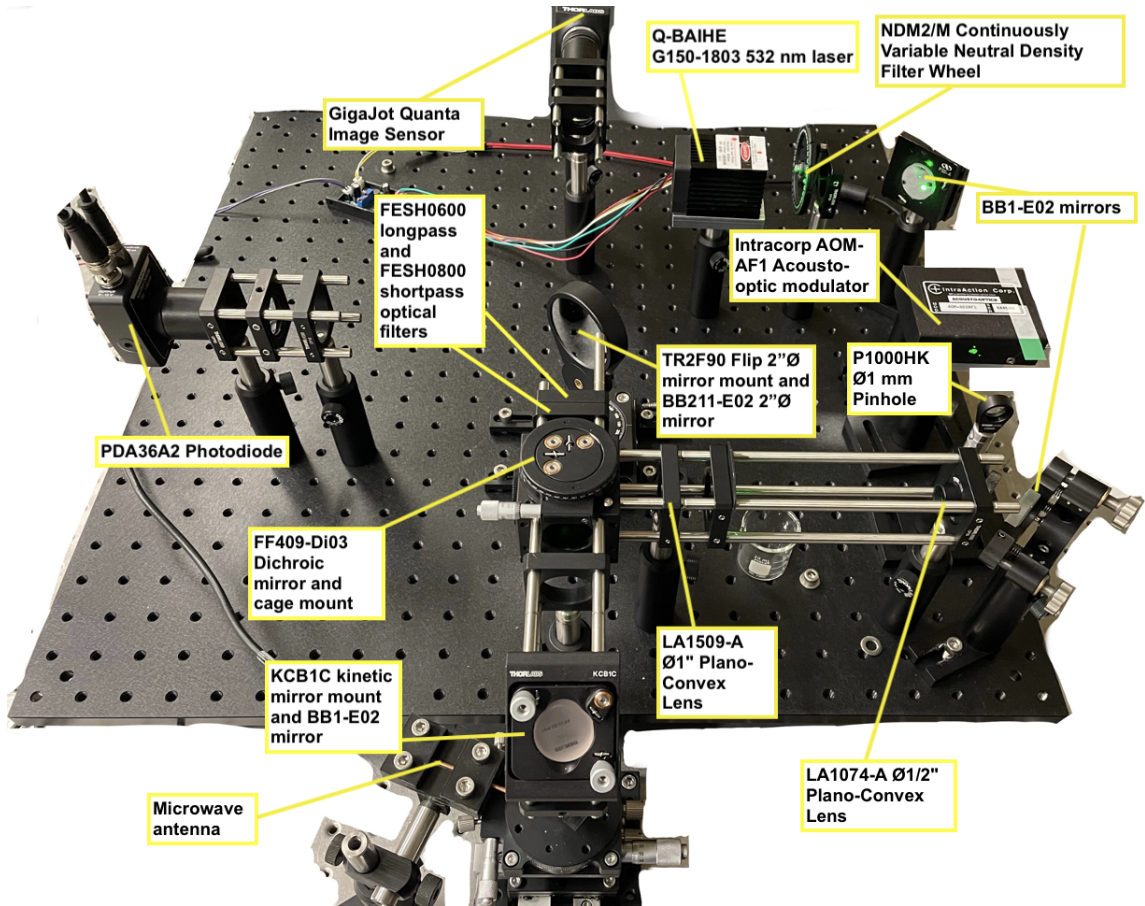


Figure 3.12: Experimental setup modified for T_1 decay experiment

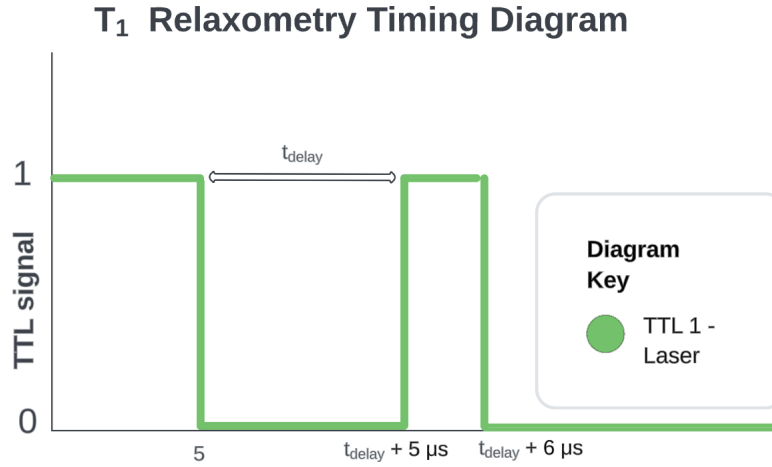
3.4.3 T_1 experimental protocol

The procedure for the experiment is as follows:

1. A laser pulse with a duration of $t_{\text{initialize}} = 5 \mu\text{s}$ is utilized to polarize and initialize the spins to a zero state.
2. The laser is turned off for a variable time delay (t_{delay}), allowing the NV centers to relax towards an equilibrium state. This state is a mixture of different states, including 0, +1, and -1.

3.4 T_1 Decay Measurement

3. The laser is pulsed for $t_{\text{read out}} = 1 \mu\text{s}$. This laser pulse is used to read the current state of the spins.



The number of recorded photons will correspond to the ratio of NV centers in the $|0\rangle$ state compared to the $|\pm 1\rangle$ state among all members of the ensemble. The brightness of the NV is expected to decrease, up to a certain point, as t_{delay} increases. By analyzing the relationship between the emitted fluorescence and the delay time, a curve of best fit can be used to estimate the decay parameter T_1 .

3.4.4 T_1 experimental results

The data was collected using the Quanta Image Sensor and its associated Python software. The QIS is an array of photodetectors, each sensitive to a single photon [2]. This means that it can count one photon at a time, and thus the exact number of photons emitted from the NV center can be measured (compared to a proportional voltage by the photodiode). Image capturing could be easily integrated into a MATLAB script by calling the QIS' Python scripts. As shown in the T_1 code in

3.4 T₁ Decay Measurement

the appendix 6.4.2, a time delay ranging from 100 μ s to 4000 μ s was utilized, with a step size of 100 μ s. Starting at 100 μ s, three trials would be run at that specific time delay. Through the use of a helper function, also included in the appendix, the average number of photons for the ten data samples would be calculated. The delay time (x) and corresponding number of photons (y) would be written into the first two columns of an Excel spreadsheet. The standard deviation would also be calculated and written into the third column of the spread sheet in the same row as the other two values. The protocol was run three times with identical parameters. Using another script, the time delay and average number of photons from the completed Excel sheet were plotted as a scatter plot in MATLAB. The standard deviation values obtained from the Excel spreadsheet were plotted using the errorbar function in MATLAB overlaying the scatterplot. Finally, the MATLAB curve fitting toolbox was used to generate a line of best fit for the plot. This line of best fit and the corresponding confidence bounds were plotted.

The T₁ decay curve displays exponential behavior and can be expressed as: $P(t) = a * e^{\frac{-t}{b}} + c$, where $P(t)$ represents the population of the excited state at time t . In this equation, a denotes a proportionality factor measured in number of photons, b represents the T₁ value in microseconds, and c represents the initial fluorescence at $t=0$, also measured in number of photons. After creating a line of best fit, the following coefficients were derived: For the QIS, the derived coefficients were: $a = 4.38 \times 10^{10}$ (number of photons); $b = 339.2 \mu\text{s}$ (T₁ decay time); $c = 7.76 \times 10^{11}$ (amount of photons). Meanwhile, the goodness of fit was found to be: R-squared = 0.971 and RMSE = 1.63×10^9 . Thus, based on the MATLAB curve of best fit, we can calculate the T₁ relaxation value to be approximately 339.2 μs . The 95% confidence bounds

3.4 T_1 Decay Measurement

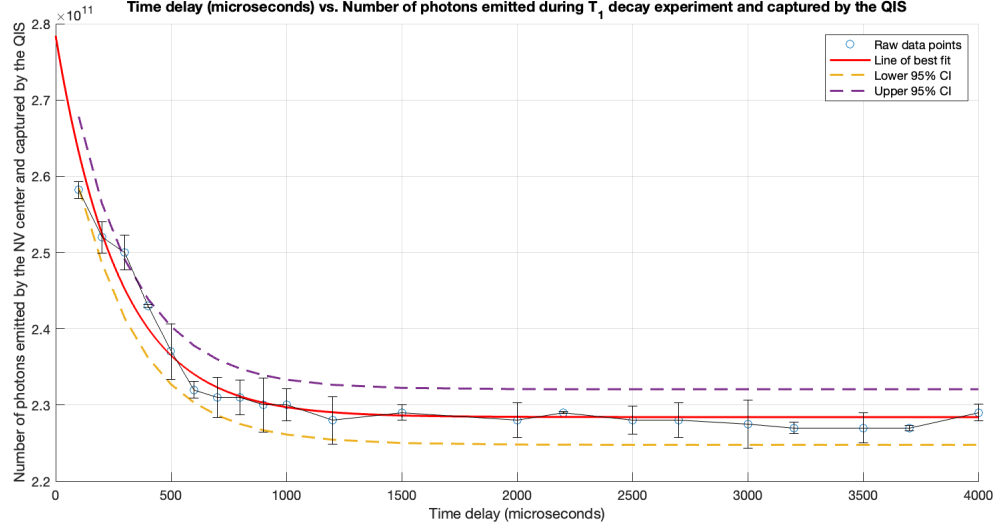


Figure 3.13: The T_1 decay curve of an NV center recorded via the Quanta Image Sensor

for the T_1 value are 279.5 μs to 399.0 μs .

3.4.5 T_1 Experimental Analysis

The T_1 decay time of an NV center in diamond will vary depending on specific experimental conditions such as temperature and magnetic field. However, typical T_1 values for NV centers in diamond are on the order of microseconds. The T_1 relaxation time in this experiment was found to be approximately 339.2 μs , which falls within a similar range to the results reported by Song et al. (1-73.6 μs) and Volkova et al. (162 μs) [21] [22] as shown in Table 5.1. In contrast, Sewani et al. and Mrózek et al. observed substantially longer T_1 decay times of approximately 1640 and 3140 μs , respectively [19] [11].

Volkova et al. provided an explanation for the shorter T_1 decay time [22], largely attributing the significant difference in T_1 to the material composition of the dia-

3.4 T_1 Decay Measurement

Table 3.1: Comparison of T_1 data collected across various papers

| Song [21] | Volkova [22] | Lasonde | Sewani [19] | Mrózek [11] |
|--------------------|--------------------------|---------------------|--------------------|--------------------|
| 73.6 μs | $162 \pm 11 \mu\text{s}$ | 339.2 μs | 1640 μs | 3140 μs |

mond sample. In general, there are two common methods for creating NV centers in diamond. The first method is intended for diamonds that already have a naturally high concentration of nitrogen impurities (up to 0.3%) [16] [20]. This method, known as high-pressure high-temperature (HPHT), involves irradiating the sample with electrons and then subjecting it to high-temperature annealing.

The second method, known as Condensed Vapor Deposition (CVD), is aimed at producing purer diamonds, often synthetic [16] [20]. In this method, high-energy nitrogen ions are implanted into the sample, followed by high-temperature annealing. Usually, HPHT is preferred over CVD due to its lower cost and time requirements [20]. The second method is also known to be more error-prone, leading to unwanted side effects such as electron spin resonance shift and linewidth broadening [20].

Notably, Volkova's T_1 decay measurement was in regard to a diamond sample fabricated using the second method - high-energy nitrogen ion implantation - by the producer Element Six. Volkova argues in her paper that the shorter than expected T_1 value could be due to rapidly fluctuating paramagnetic defects in the vicinity of the nitrogen-vacancy centers, as well as potential interactions between the electron spins [22]. This raises the possibility that an unintended side effect may have occurred during the creation of her sample [20]. Interestingly, Volkova reports only up to 10^7 photon counts per second without an ND filter [22]. However, when using an ND filter to decrease the power of the laser by 66%, this experiment found counts closer to 10^{11} emitted photons per second. It is estimated that NV centers emit around

3.4 T₁ Decay Measurement

2.5×10^8 billion photons per second, which implies either a great concentration of NV centers were in the sample used in the experiment or increased sensitivity of the image sensor [1].

Moreover, Song [21] also utilized a nitrogen vacancy center synthesized through chemical vapor deposition (CVD) to achieve a T₁ read out of 73.6 μ s. In their paper [20], Song states that the surface spin density of HPHT nanodiamonds (NDs) is two orders of magnitude higher than that of bulk single-crystal CVD diamond and CVD diamond thin-film, as reported in two recent studies [18] and [12]. Thus, Song has implied that in the future, they will shift away from diamonds treated with chemical vapor deposition (CVD) to nanodiamonds produced through high-pressure, high-temperature methods.

On the other hand, both Sewani [19] and Mrózek [11] uses a HPHT diamond in their studies. In the appendix, it is revealed that Sewani took measurements to compare their HPHT diamond with a CVD diamond purchased from Element Six. Despite conducting identical tests, the photoluminescence emitted by the HPHT diamond was 705 nW, while that emitted by the CVD diamond was only 0.75 nW. Although the increased nitrogen density played a significant role, the HPHT diamond was used to conduct tests resulted in a T₁ value of 1640 μ s.

Mrozek also utilized a sample of HPHT-synthesized diamond [11], and there is a clear figure provided in his work as well that demonstrates a direct correlation between an increase in nitrogen concentration (measured in parts per million) and a decrease in T₁ decay time [11]. It is possible that the nitrogen concentration in a sample may have a greater impact on the length of T₁ time than the synthesis process.

Chapter 4

Control protocols

4.1 Microwave manipulation of an NV center

Although laser light is a powerful tool for initializing and reading the spin state of NV centers, it cannot be used to coherently manipulate the spin state of an NV center. Instead, microwave signals with a specific duration and frequency can be utilized to control the excitation of an NV center from its ground energy state. In tandem, laser light and microwave pulses can be used to intentionally manipulate and read the state of an NV center.

There are two microwave pulses with specific durations and frequency that are used to manipulate the state of an NV center. The first type of pulse is a π pulse, which is used to excite an NV center from the ground state $|0\rangle$ to the excited state $|+1\rangle$ or $|{-1}\rangle$, depending on the frequency. The second type of pulse, a $\pi/2$ pulse, is used to transition an electron from the $|0\rangle$ state to the superposition of $\frac{1}{\sqrt{2}}(|0\rangle + |+1\rangle)$ or $\frac{1}{\sqrt{2}}(|0\rangle + |{-1}\rangle)$.

To understand the purpose and meaning of π and $\pi/2$, consider a Bloch sphere.

4.1 Microwave manipulation of an NV center

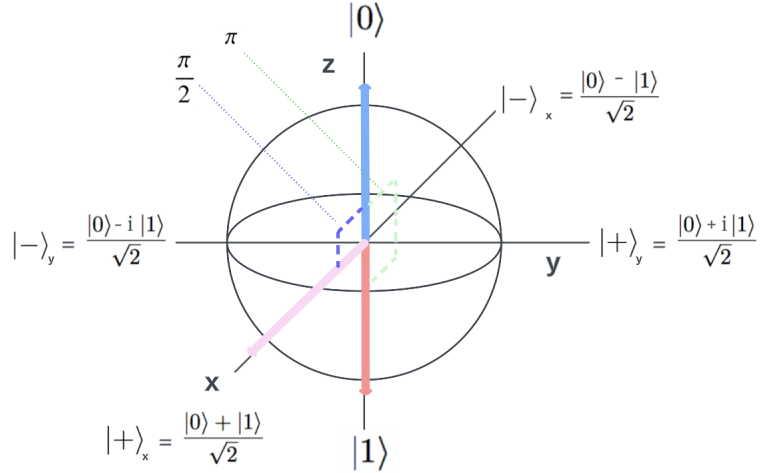


Figure 4.1: Bloch sphere representing the directionality of an NV center spin

As shown in Figure 4.1, a Bloch sphere is a graphical representation used to visualize the spin state of an NV center. Specifically, a point inside or on the surface of this sphere represents the state of NV center as a qubit. This point on the sphere is described by two angles, often denoted as θ , the polar angle ranging from 0 to π , and ϕ , the azimuthal angle ranging from 0 to 2π . A general quantum state of a qubit can be expressed as $\cos(\theta/2)|0\rangle + e^{i\phi}\sin(\theta/2)|1\rangle$. Here, the $|0\rangle$ and $|1\rangle$ states correspond to the north and south poles of the sphere, respectively. The factor $e^{i\phi}$ represents a phase shift, while the terms $\cos(\theta/2)$ and $\sin(\theta/2)$ describe the probability amplitudes for the states $|0\rangle$ and $|1\rangle$, respectively.

Thus, a $\pi/2$ microwave pulse, applied to an NV center for a specific duration, is utilized to rotate the spin state of the NV center by 90 degrees ($\pi/2$ radians) around a particular axis in the Bloch sphere (e.g., from the blue arrow to the light pink arrow). This pulse creates a superposition of the $m_s = 0$ and $m_s = +1$ states. On the other

4.2 Pulsed ODMR spectra

hand, a π microwave pulse (again with a specific duration) will rotate the spin state of an NV center by 180 degrees (or π radians) around the same axis in the Bloch sphere (e.g., the blue arrow to the coral arrow).

It is important to note that the Bloch Sphere is depicts a two-level systems, while the NV center is inherently a three-level system. In this way, the use of a Bloch Sphere could be misleading, as it oversimplified the characteristics of the NV center.

4.2 Pulsed ODMR spectra

The pulsed optically detected magnetic resonance (ODMR) experiment for an NV center is an alternative approach to the continuous-wave (CW) ODMR method. In pulsed ODMR, both microwave and optical pulses are utilized to manipulate and read out the spin state of the NV center, instead of using continuous laser excitation and read out in the CW ODMR experiment.

The purpose of the pulsed ODMR experiment is to determine the resonant microwave frequency for transitions between sublevels with greater precision than CW ODMR using microwaves [6]. The pulsed nature of the technique helps to reduce background noise, leading to a higher signal-to-noise ratio and improved sensitivity [6].

4.2.1 Pulsed ODMR experimental setup

To begin with, the experimental setup was modified from the T₁ experiment by adding an extra RF source, switch, and TTL line. The RF source utilized in this study was the Windfreak SynthUSBII (34MHz – 4.4GHz) RF Signal Generator, which was

4.2 Pulsed ODMR spectra

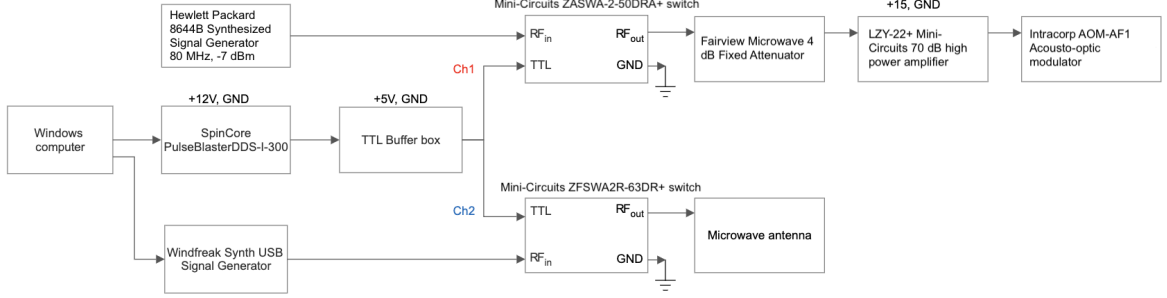


Figure 4.2: Experimental non-optical setup with further detail

connected to a Mini-Circuits ZFWA2R-63DR+ (0.5-6 GHz) switch controlled by the TTL lines. The TTL line was constructed by soldering the output of the SpinCore board to a coaxial cable. The other end of the coaxial cable was then soldered to a BNC adapter, which allowed for interfacing with the SpinCore buffer box.

In the appendix, a highly detailed description of the experiment's setup and preparation, including the names of all components, will be provided. Although verbose, this explanation offers a more comprehensive understanding of the human-centered instructions necessary to operate the spectrometer and conduct the experiment. The details of the pulsed ODMR experiment, including timing, will be included in this chapter.

4.2.2 Pulsed ODMR experimental procedure

The experimental protocol for pulsed ODMR includes initializing the NV center's spin state with a short laser pulse, applying a microwave pulse at a specific frequency to manipulate the spin state, and using a second laser pulse to read out the spin state through fluorescence detection. By repeating these steps multiple times and varying the microwave frequency, a comprehensive ODMR spectrum can be constructed.

4.2 Pulsed ODMR spectra

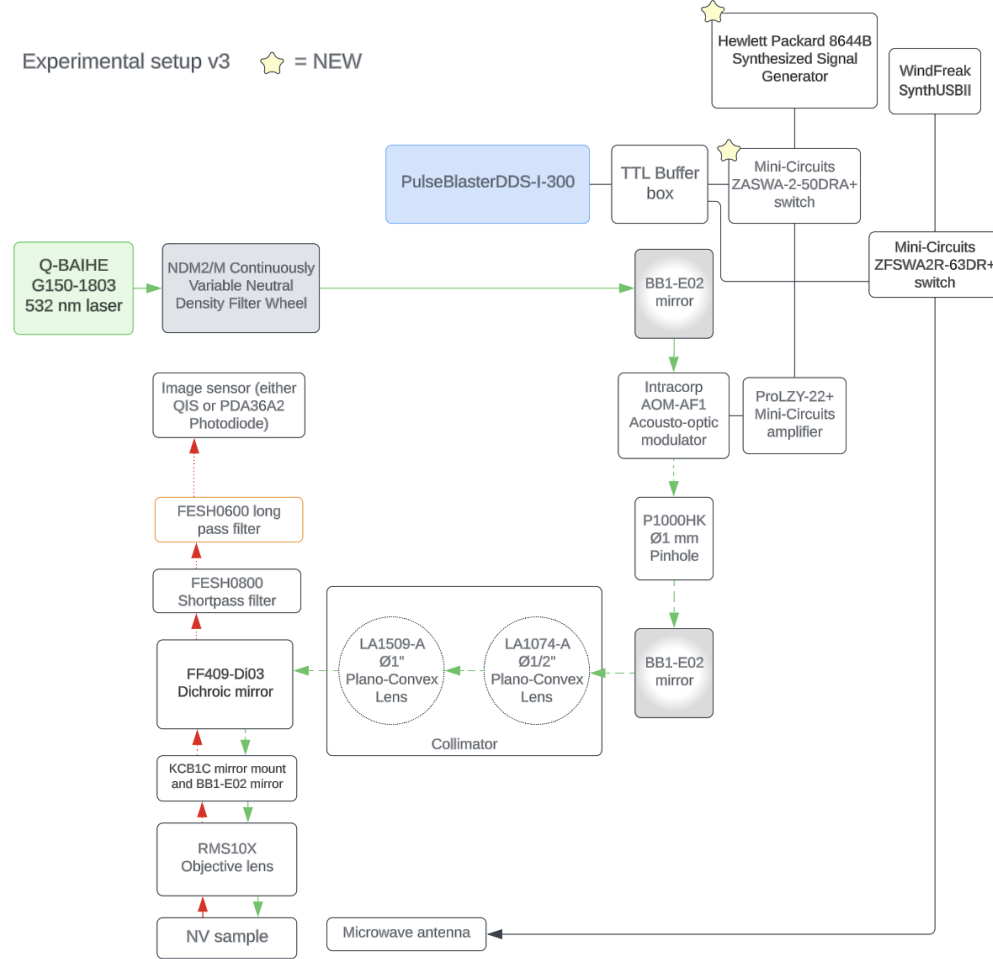


Figure 4.3: Third iteration of the experimental setup, a star denotes an addition since the second iteration

1. A laser signal is turned on for 5 μ s to initialize the NV center into the $|0\rangle$ state.
2. No signal is applied for 5 μ s.
3. A microwave pulse of 5 μ s is applied to the field.
4. No signal is applied for 2 μ s as padding before read out.
5. A second laser signal is turned on for 5 μ s to trigger fluorescence for data

4.2 Pulsed ODMR spectra

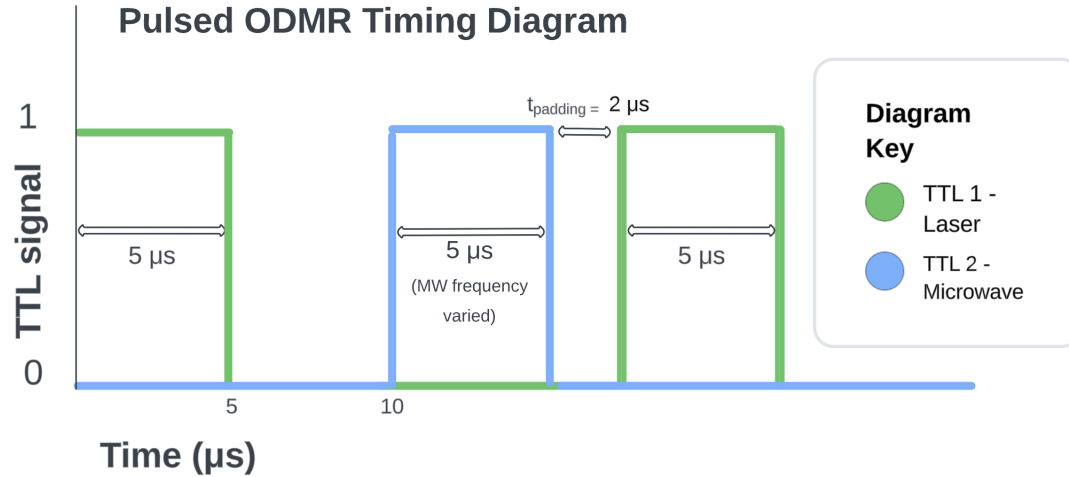


Figure 4.4: Pulsed ODMR timing diagram

collection.

The steps of this experiment were then repeated, with the microwave frequency being changed thirteen times between 2810 MHz and 2900 MHz. Three samples were taken for each frequency at which data was collected.

4.2.3 Pulsed ODMR Experimental Results

Once the data was collected, the three points per frequency were averaged, and then a scatter plot was created and presented in Figure 4.5. The standard deviation of those three samples was also calculated via Excel. Red error bars corresponding to the standard deviation are also overlaid on the graph. Each data point had an average standard deviation of 4.67 mV.

The plot below shows the results of varying the microwave pulse frequency of an NV center. The y-axis records voltage, which is proportional to fluorescence, or the

4.2 Pulsed ODMR spectra

number of emitted photons. The x-axis represents the microwave frequency.

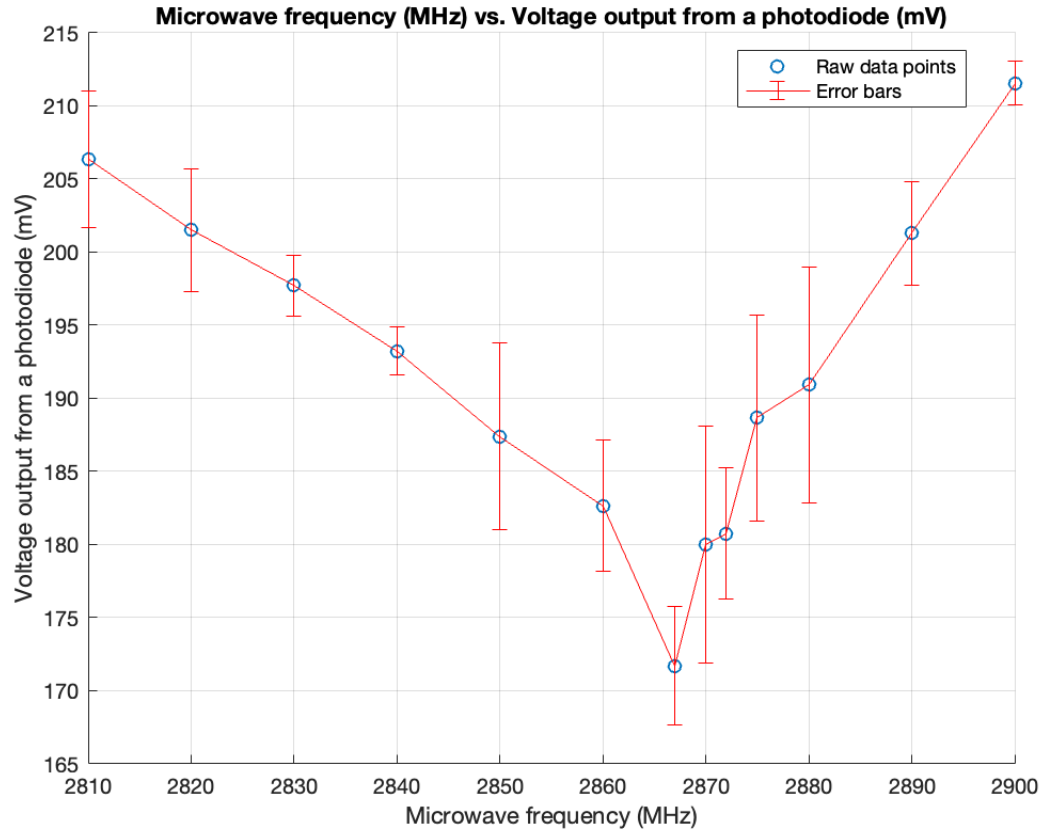


Figure 4.5: Pulsed ODMR experimental results recorded via the Thorlabs photodiode

4.2.4 Pulsed ODMR experimental analysis

From the graph above, it is evident that there is a notable decrease in fluorescence when the microwave frequency is at approximately 2870 MHz. It is important to note that there is only one dip in this ODMR spectrum, as opposed to the CW ODMR spectrum shown in Figure 3.9. In this experiment, no external magnetic field was used to lift the degeneracy between the $m_s = +1$ and $m_s = -1$ sublevels. Thus, the dip in Figure 4.5 corresponds to a combination of resonant transitions between the

4.3 Rabi Oscillation Measurement

spin states $m_s = 0$ and $m_s = \pm 1$.

As mentioned in Chapters 2 and 3, the fluorescence of an NV center is related to its spin state. When the microwave frequency resonates with the spin state transitions, the population of the $m_s = 0$ sublevel decreases while the population of the $m_s = \pm 1$ sublevels increases. This results in an overall increase in the probability of non-radiative relaxation, which subsequently decreases the fluorescence intensity detected during the read out laser pulse. It is now understood that future experimental protocols involving microwave pulses should be conducted at a frequency of 2.87 GHz to achieve optimal control of spin-state transitions.

4.3 Rabi Oscillation Measurement

4.3.1 Rabi oscillation experimental setup

Rabi oscillations can be observed through the fluorescence signal that oscillates in correspondence with the electronic spin states of an NV center exchanging between the ground and excited states [19]. This oscillatory behavior indicates that the coherent transfer of electrons between the ground and excited states. By plotting the oscillations, one can calculate the optimal durations of microwave pulses. By determining these durations, purposeful manipulation of the NV center can be achieved.

There were no major setup changes required for the Rabi oscillation experiment, unlike the pulsed ODMR experiment. The only changes made were related to the timing of the laser and microwave pulse sequence. Now, the microwave frequency is kept constant at 2.87 GHz, which has been confirmed to be the resonant frequency

4.3 Rabi Oscillation Measurement

for the $m_s = \pm 1$ states. The purpose of the Rabi oscillation experiment is to determine the duration of a microwave pulse at its resonant frequency that generates the maximum number of emitted photons. The new timing procedure is shown in Figure 4.6 and will be briefly described below.

1. A laser signal is turned on for 5 μs to initialize the NV center into the $|0\rangle$ state.
2. No signal is applied for 5 μs .
3. A microwave pulse with a frequency of 2.87 GHz is applied for a variable duration ranging from 0.05 to 3 μs .
4. No signal is applied for 2 μs as padding before read out.
5. A second laser signal is turned on for 5 μs to trigger fluorescence for data collection. The population of the excited state is measured after each pulse.

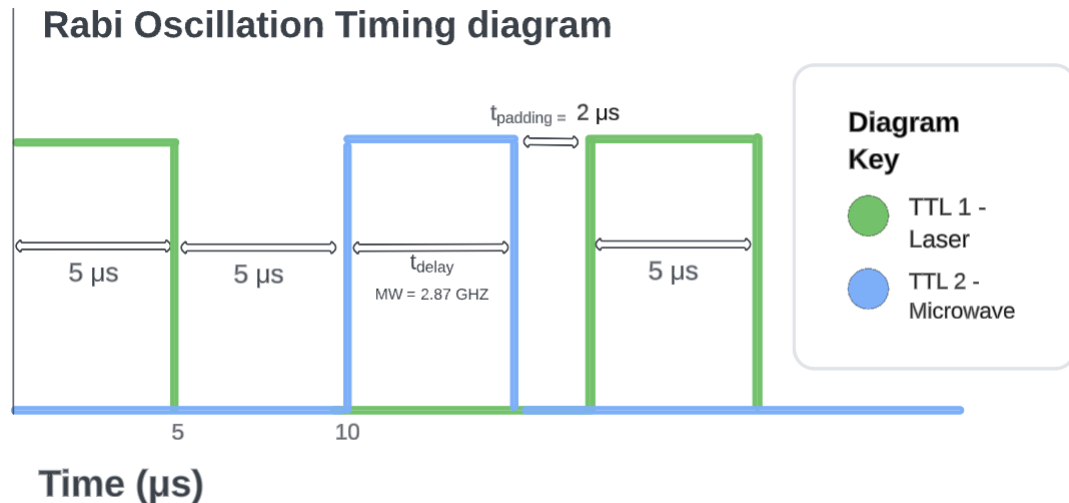


Figure 4.6: Rabi oscillation timing diagram

4.3 Rabi Oscillation Measurement

4.3.2 Rabi oscillation experimental results

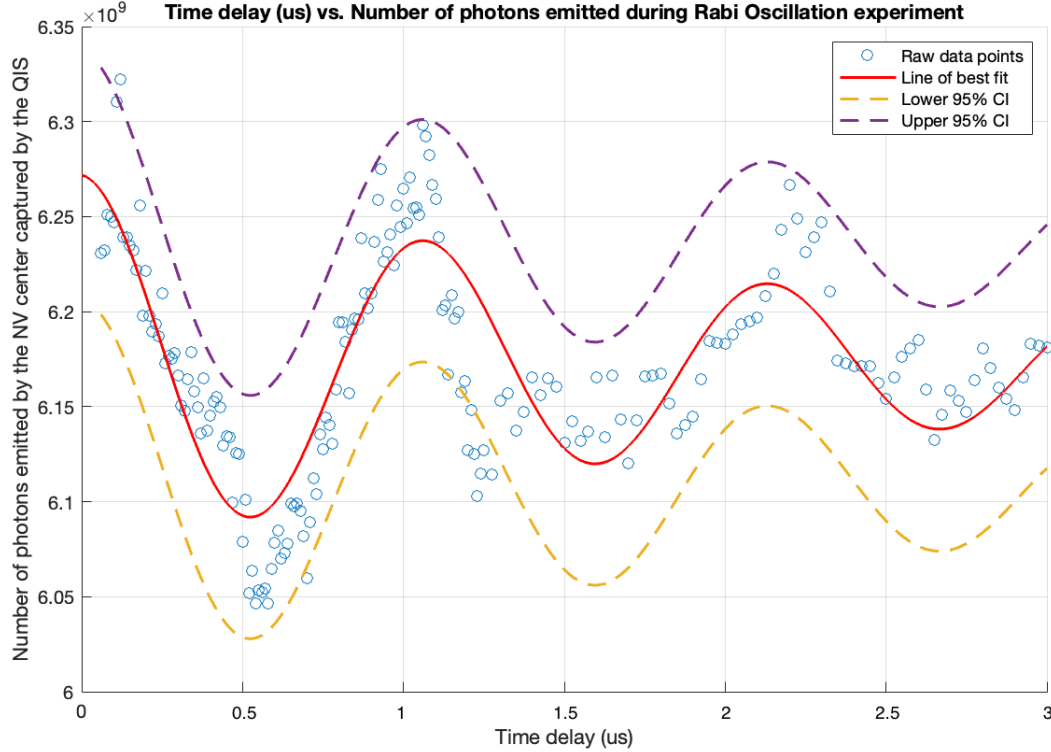


Figure 4.7: Rabi experimental results recorded via the Quanta Image Sensor

The data was collected using the Quanta Image Sensor and its associated Python software. Image capturing could be easily integrated into a MATLAB script by calling the QIS' Python scripts. As shown in the Rabi oscillation code in the appendix 6.4.4, a time delay ranging from 0.05 microseconds to 3 microseconds was utilized, with a step size of 0.05 microseconds. For each step, the delay time (x) and corresponding number of photons (y) would be written into the first two columns of an Excel spreadsheet. Using another script, the time delay and number of photons from the Excel sheet were plotted as a scatter plot in MATLAB. Finally, the MATLAB curve fitting toolbox was used to generate a line of best fit for the plot. This line of best fit and the

4.3 Rabi Oscillation Measurement

corresponding confidence bounds were plotted.

4.3.3 Rabi Oscillation Experimental Analysis

The data collected from the Rabi oscillation experiment is shown in Figure 4.7. The data reveals two 'peaks' of an increased number of emitted photons, which gives the overall impression of a damped oscillation. The first peak occurs when the 2.87 GHz microwave pulse lasts for 1.20 μ s, while the second peak occurs at 2.40 μ s. The duration of the microwave pulse tested ranged from 0 to 3 μ s. A total of 194 data points were collected within these two bounds. Based on this data, a line of best fit was determined using the MATLAB curve fitting tool. The coefficients for the damped cosine equation, $a * \cos(\omega * x) * e^{\frac{-x}{b}} + d$, are as follows: $a = 9.948 \times 10^7$ (number of photons), $b = 2.7$ (μ s), $d = 6.173 \times 10^9$ (number of photons), and $\omega = 0.005864$ (rad/s). Additionally, the coefficients for the 95% confidence bounds of the model are: $a [8.328 \times 10^7, 1.157 \times 10^8]$, $b [1.496, 3.504]$, $d [6.168 \times 10^9, 6.177 \times 10^9]$, and $\omega [0.005768, 0.005962]$. The R-squared value and RMSE are 0.59 and 2.6×10^7 .

In this equation, the variable b represents the inverse of the damping coefficient. In this particular case, b is also referred to as the T_2^{Rabi} decay constant. Specifically, the T_2^{Rabi} coherence time describes how long the ensemble's $|0\rangle_g \leftrightarrow |1\rangle_g$ transition can be driven before it dephases into a mixed state [19]. In this experiment, the value of T_2^{Rabi} was determined to be 2.70 μ s. Although the T_1 decay values found in this paper were much shorter than the T_1 value reported in Sewani's paper [19], Sewani's paper found that the T_2^{Rabi} was approximately 1.12 μ s. This value is approximately half the length of the one reported in this paper. This phenomenon of T_1 discrepancies caused by changes in diamond sample composition, does not affect the T_2 decay time.

4.4 Hahn Echo (T_2 decay) measurement

4.3.4 Analysis of π and $\pi/2$ pulses

To calculate the values of π and $\pi/2$, the following equations can be used:

$$t_\pi = \frac{\pi}{\omega} \text{ and } t_{\frac{\pi}{2}} = \frac{t_\pi}{2}$$

Plugging in the value of ω calculated from the curve of best fit above, we have:

$$t_\pi = \frac{\pi}{\omega} = \frac{\pi}{0.005864} = 536 \text{ ns and } t_{\frac{\pi}{2}} = \frac{t_\pi}{2} = 268 \text{ ns}$$

The application of the π and $\pi/2$ pulses will be demonstrated in the following experiment. The durations of the π and $\pi/2$ pulses reported in Sewani's paper were 144 ns and 72 ns, respectively.

4.4 Hahn Echo (T_2 decay) measurement

The T_2 time is a measurement of the coherence of the NV center as a quantum system. Unlike T_1 relaxation, which involves the exchange of energy between the quantum system and its environment, T_2 relaxation is primarily caused by dephasing. Dephasing is a phenomenon in which external factors cause the quantum spin state of the NV center to lose coherence. Furthermore, the T_2 time is always less than or equal to the T_1 time ($T_2 < T_1$).

4.4.1 Hahn Echo (T_2 decay) Experimental Setup

The Hahn Echo experimental setup involves no physical changes compared to the Rabi Oscillation experimental setup. The main difference between the two exper-

4.4 Hahn Echo (T_2 decay) measurement

imental protocols is that the Hahn Echo experiment employs a sequence of three microwave pulses: a $\pi/2$ pulse, followed by a π pulse, and then another $\pi/2$ pulse [16].

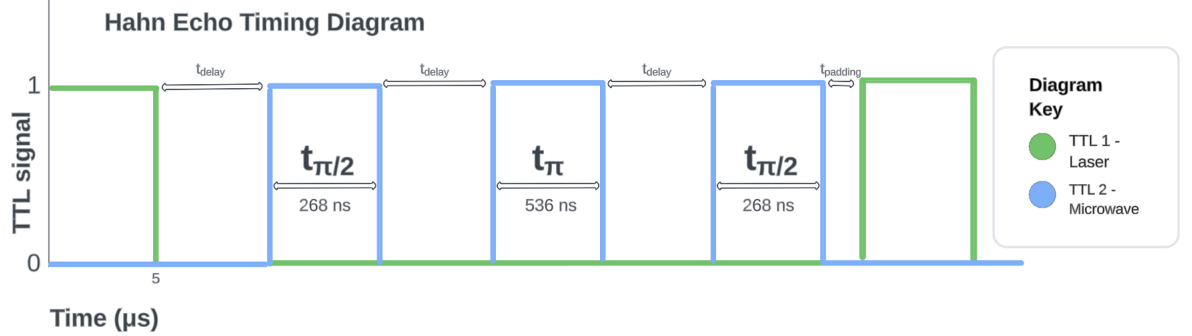


Figure 4.8: T_2 timing diagram

1. **Initial state and the first $\pi/2$ pulse:** The initial state of the NV center is aligned with the z-axis. The first $\pi/2$ pulse acts as a rotation operator, which rotates the NV center's spins by 90 degrees around the Bloch sphere to the positive x-axis (see Figure 4.1 above). This creates a coherent superposition of the triplet spin states between sublevels.
2. **Free evolution:** Following the first pulse, the system is allowed to evolve freely for 2 μs. The spin states precess due to local magnetic fields, which results in a spreading of the phase of the states, known as dephasing.
3. **The π pulse:** A subsequent π pulse is then applied, which inverts the spin states around the negative x-axis, effectively reversing the direction of their phase evolution.

4.4 Hahn Echo (T_2 decay) measurement

4. **Second free evolution:** After another 2 μs , the states begin to reconverge as they evolve in the opposite direction.
5. **Final $\pi/2$ pulse and read out:** Finally, another $\pi/2$ pulse is applied to return the spins to their initial position along the z-axis. This operation transforms the coherence back into population difference, which can then be measured.

In this process, despite the NV centers having different local fields leading to different precession frequencies, the application of the π pulse refocuses the spins. This results in them returning to the same point in phase space at the same time, creating what is known as a spin echo. The refocusing mechanism used in the experiment helps to preserve the coherence of the quantum information for extended periods. This refocusing mechanism would be highly useful for the realization of qubits.

4.4.2 Hahn Echo (T_2 decay) Experimental Results

The data was collected using the Quanta Image Sensor and its associated Python software. Image capturing could be easily integrated into a MATLAB script by calling the QIS' Python scripts. As shown in the T_2 code in the appendix 6.4.2, a time delay ranging from 0.1 microseconds to 4 microseconds was utilized, with a step size of 0.1 microseconds. For each step, the delay time (x) and corresponding number of photons (y) would be written into the first two columns of an Excel spreadsheet. Using another script, the time delay and number of photons from the Excel sheet were plotted as a scatter plot in MATLAB. Finally, the MATLAB curve fitting toolbox was used to generate a line of best fit for the plot. This line of best fit and the corresponding confidence bounds were plotted.

4.4 Hahn Echo (T_2 decay) measurement

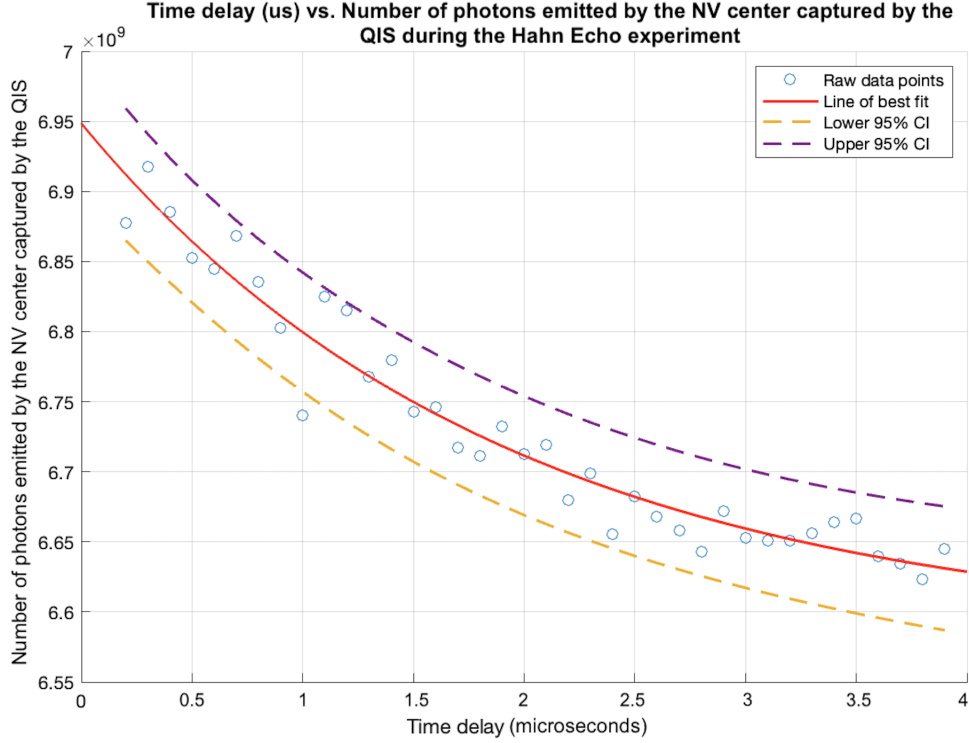


Figure 4.9: Hahn Echo experimental results recorded via the Quanta Image Sensor

The T_2 decay curve exhibits exponential behavior and can be mathematically represented as: $P(t) = a * e^{-\frac{t}{b}} + c$, where $P(t)$ denotes the population of the excited state at time t . In this equation, a represents a proportionality factor measured in number of photons, b represents the value of T_2 measured in nanoseconds, and c represents the initial fluorescence at $t=0$, also measured in number of photons. After creating a line of best fit, the following coefficients were derived: $a = 3.643 \times 10^8$ (number of photons); $b = 1.902 \mu\text{s}$ (T_2 decay time); $c = 6.54 \times 10^9$ (amount of photons). Meanwhile, the goodness of fit was found to be: R-squared = 0.942 and RMSE = 2.03×10^7 . Thus, based on the curve of best fit calculated by the MATLAB curve fitting tool, we can calculate the T_2 relaxation value to be approximately 1.9 μs . Additionally, the coefficients for the 95% confidence bounds for the T_2 relaxation

4.4 Hahn Echo (T_2 decay) measurement

value were calculated to be 1.237 μs to 2.568 μs also with the MATLAB curve fitting tool.

4.4.3 T_2 Experimental Analysis

The T_2 time of an NV center can vary significantly depending on factors such as the quality of the diamond lattice, the presence of nearby spins, and the external magnetic field [15]. However, the typical T_2 values for NV centers in diamond are only a few microseconds, which is generally much less than the T_1 value.

Table 4.1: Comparison of T_1 and T_2 data collected across various papers

| | Song [21] | Volkova [22] | Lasonde | Sewani [19] |
|-------|-----------------------|----------------------------|-------------------|--------------------|
| T_1 | 73.6 μs | $162 \pm 11 \mu\text{s}$ | 339 μs | 1640 μs |
| T_2 | 0.1-2.7 μs | $.560 \pm .05 \mu\text{s}$ | 1.9 μs | 1.2 μs |

The T_2 dephasing time of an NV center, as reported by Song et al., fell within a range of 0.1-2.7 μs [21]. Meanwhile, Sewani et al. and Volkova et al. reported 1.2 μs and $0.560 \pm 0.05 \mu\text{s}$, respectively [19] [22]. All researchers appear to report similar values of the T_2 decay time of an NV center in diamond.

Chapter 5

The QIS vs. CMOS Analysis

5.0.1 Overview of Image Sensors

At the focal point of a 1 mW laser beam, a single NV center can emit approximately 10^7 red photons per second [23]. Although an incredibly large number, fluctuations in the number of photons correspond to relatively small changes in fluorescence. It is estimated that the ODMR experimental protocol depends on detecting small changes of 5-10%. Therefore, it is important for the stability of both the laser's power and the image sensor's sensitivity.

In this experimental thesis, both the Gigajot Quanta Image Sensor (QIS) and the Thorlabs PDA36A2 photodiode were utilized as image sensors. The QIS is an array of photodetectors, each sensitive to a single photon [2]. This means that it can count one photon at a time. A binary measurement of either '0' (indicating no photon) or '1' (indicating one photon) is then outputted. This enables the QIS to capture images or optically scan small cavities, such as NV-centers, with minimal interference. By reducing the noise in the system, the QIS would immensely improve the scalability of

The QIS vs. CMOS Analysis

NV centers as quantum sensors and quantum bits, as compared to their usage with a CMOS image sensor.

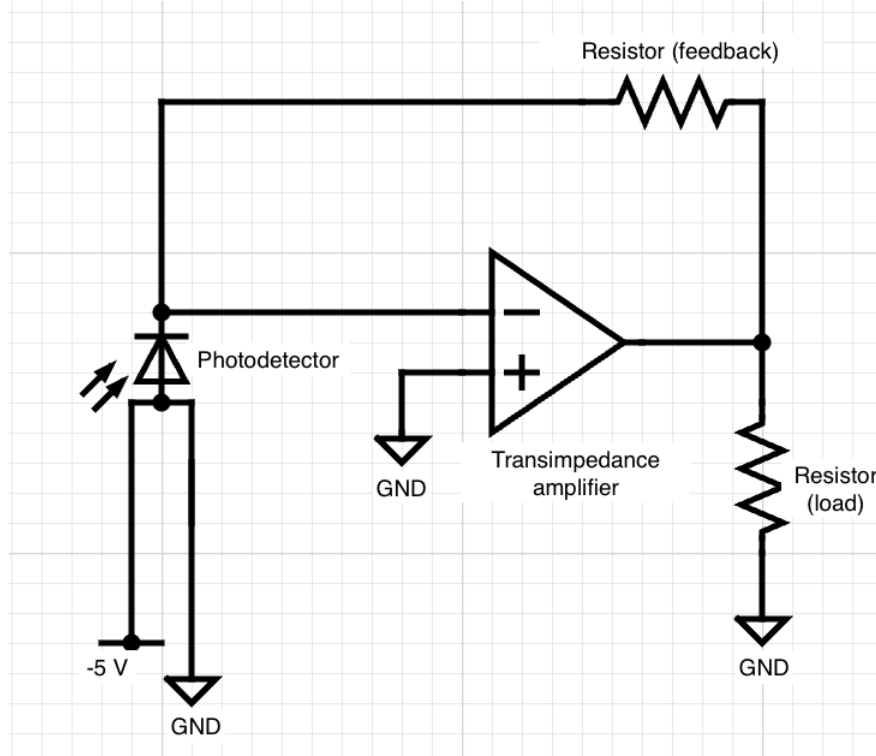


Figure 5.1: Thorlabs PDA36A2 photodiode schematic

The PDA36A2 photodiode is a silicon detector that is amplified and has switchable gain. It is specifically designed to detect light signals within the range of 350 to 1100 nm. The schematic diagram of the photodiode, which includes the reverse-biased photodiode and transimpedance amplifier for gain, is illustrated in Figure 5.1. In both the T₁ and T₂ experiments using the photodiode, the switchable gain setting was set to 20 dB to ensure that the bandwidth of the photodiode was sufficient for the experiments. It is crucial to note that amplifying this photodiode does not necessarily result in a more accurate measurement. However, without external amplification, it would not have been possible to detect the change in the number of emitted photons

The QIS vs. CMOS Analysis

from the NV center. The photodiode was amplified using the Stanford Research Systems SR560 low-noise preamplifier at a setting of 500x.

| | Cleveland QIS [2] | Photodiode [14] |
|-------------------|-----------------------|--------------------------|
| Sensor type | QIS | Si Free space photodiode |
| Frame size | 20.25 mm ² | 13 mm ² |
| Frames per second | 1 MHz | 1 MHz |
| Dynamic range | 95 dB | 20 dB |
| RMS | 0.19 e- | 207 μ V |
| Offset | \pm 5.68 e- (max) | \pm 12 mV (max) |

Table 5.1: Comparison of Photodiode and QIS parameters

5.0.2 T₁ and T₂ experimental data collected via the photodiode

Throughout this thesis, quantum control protocols were employed using both the PDA36A2 photodiode and the Cleveland QIS. As the T₁ and T₂ graphs for the QIS were presented in chapter 3 and chapter 4 respectively, they will not be included in this chapter. Furthermore, the background and methodology of the T₁ decay and Hahn Echo experiments will not be explained again in this chapter. Below, in Figure 5.2 and Figure 5.3, the T₁ and T₂ curves for the photodiodes are shown. Everything in the experimental setup remained unchanged, except for the power of the green laser. The experiment with the QIS utilized an ND filter to decrease the power of the

The QIS vs. CMOS Analysis

laser by 66% (100 mW) or so.

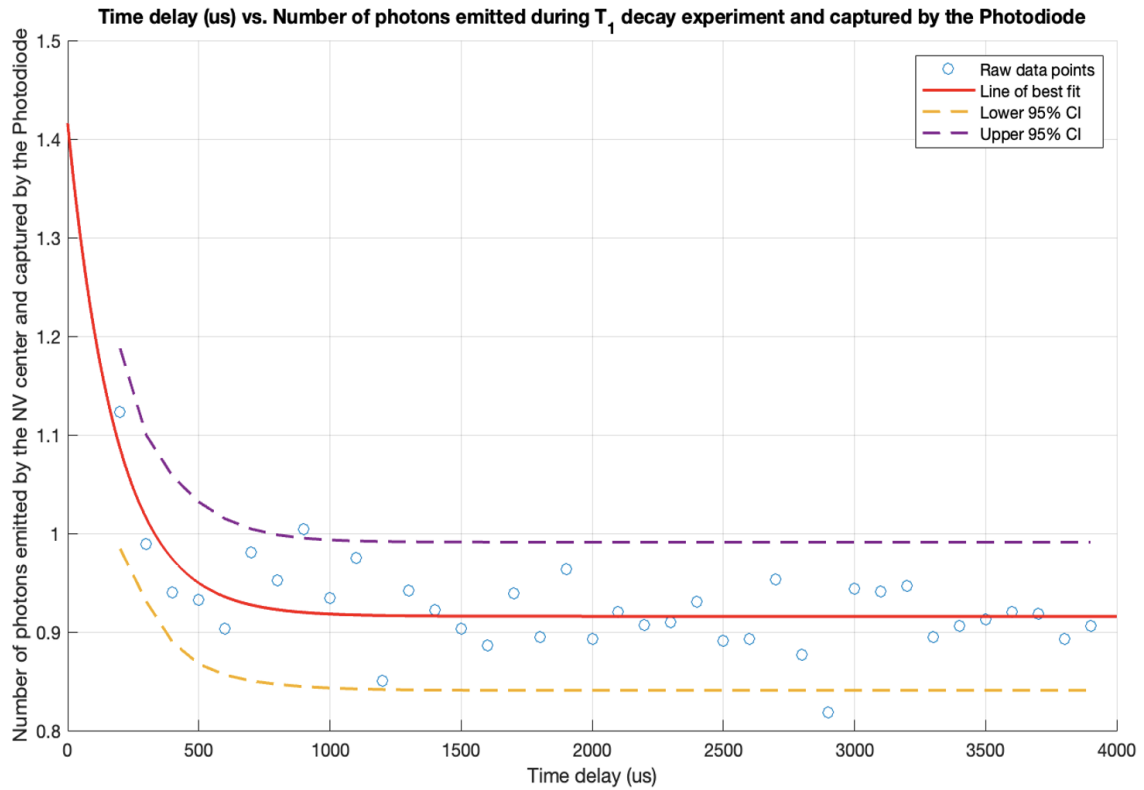


Figure 5.2: T_1 decay curve captured via the photodiode

Data from the photodiode was collected using the Picoscope's Windows software. The time delay was varied from 50 to 5000 nanoseconds, with 12 steps within that range. Four pieces of data were collected per step and then averaged using Excel. The standard deviation was calculated in Excel using those four data points. The raw data was inputted into MATLAB and plotted.

The T_1 decay curve was modeled as: $P(t) = a * e^{-\frac{t}{b}} + c$, where $P(t)$ represents the population of the excited state at time t , a is a proportionality factor indicating the number of photons, b represents the decay time or T_1 , and c represents the initial

The QIS vs. CMOS Analysis

fluorescence or number of photons. For the photodiode, the coefficients for the curve of best fit are: $a = 0.2016$ (V), $b = 362$ (μ s), and $c = 0.882$ (V). Additionally, the T_1 decay constant values at the 95% confidence bounds are 253.1 to 472 μ s. The R-squared value was 0.9743. For the QIS, the derived coefficients were: $a = 4.38 \times 10^{10}$ (number of photons); $b = 339.2$ μ s (T_1 decay time); $c = 7.76 \times 10^{11}$ (amount of photons). The R-squared value was 0.971.

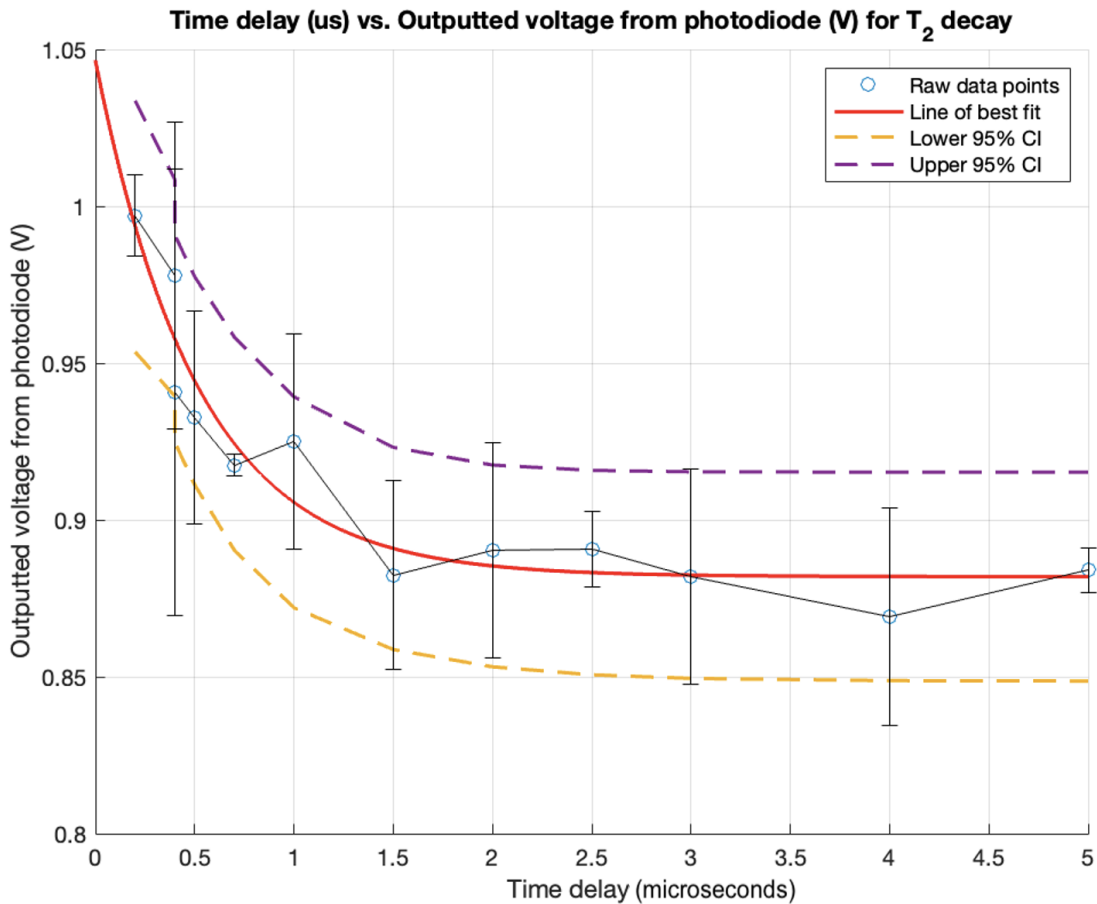


Figure 5.3: T_2 decay curve captured via the photodiode

The T_2 decay curve was also modeled as: $P(t) = a * e^{-\frac{t}{b}} + c$. For the photodiode, the coefficients for the curve of best fit are: $a = 0.164$ (V), $b = 1.93$ (μ s), and $c =$

The QIS vs. CMOS Analysis

0.8928 (V). Additionally, the coefficients for the 95% confidence bounds of T_2 decay constant are 0.785 to 3.09 μ s. The R-squared value was 0.912. Meanwhile, for the QIS, the derived coefficients were: $a = 3.643 \times 10^8$ (number of photons); $b = 1.902 \mu$ s (T_2 decay time); $c = 6.54 \times 10^9$ (amount of photons). The R-squared value was 0.942.

5.0.3 Calculations

According to the manual [14], the responsivity of the PDA36A2 photodiode is directly proportional to the wavelength of the light source. A lookup table is provided, which enables us to determine that the photodiode has a responsivity of 0.5 A/W at 700 nm. Furthermore, according to the manual, the responsivity of the PDA36A2 photodiode can be defined as the ratio of generated photocurrent (I_P) to the incident light power (P) at a specific wavelength, which can be expressed as: $R(\lambda) = I_{PD}/P$. The maximum output current is 100 mA, therefore the approximate power output is $P \approx 200$ mW.

Additionally, the equation for photon energy is $P = \Phi \times E$, where E represents the energy of the photon and is equal to $h\nu$. Here, h denotes Planck's constant, which has a value of 6.6261×10^{-34} Js. The variable ν represents the frequency of the photon, and Φ represents the photon flux. To calculate the photon flux (in number of photons per second), divide the power by $h\nu$. By using the equation $E = h\nu$, it is possible to calculate that:

$$E = 4.1357 \times 10^{-15} \text{ eVs} \times \frac{1}{700 \times 10^{-9} \text{ s}} = 0.00289 \text{ eV}$$

Now, since power is the product of flux and energy – $P = \Phi \times E$, we can say

The QIS vs. CMOS Analysis

$\Phi = \frac{P}{E}$. Thus, plugging in:

$$\Phi = \frac{0.2 \text{ W}}{0.00289 \text{ eV}} \times \frac{1 \text{ eV}}{1.602 \times 10^{-19} \text{ Ws}} = 4.32 \times 10^{20} \frac{\text{photon}}{\text{s}}$$

For intervals of 1 μs , the anticipated number of photons would be 4.32×10^{14} photon/ μs .

5.0.4 Analysis

Based on the data from both experiments and sensors, the following observations can be made:

1. The QIS detected a longer T_1 relaxation time than the photodiode.
2. The QIS provided tighter confidence bounds and a slightly higher R-squared value for the T_1 relaxation time.
3. Despite being subjected to only 1/3rd of the brightness that the Photodiode was, the QIS demonstrated a higher proportionality factor (a).

The superior sensitivity of the QIS to longer decay times, its consistency, and potential sensitivity to changes in photon count suggest that the QIS is the more suitable sensor for NV center quantum sensing. These advantages make the QIS a better option for this application. Being able to distinguish between small differences in counts is not always necessary to differentiate between two states in an ensemble. However, given a single NV center, this could change dramatically. Especially if centers were coupled, in theory, it would be possible for a single QIS to detect multiple streams of photons from individual centers. Granted, the optics of this setup would be incredibly advanced.

The QIS vs. CMOS Analysis

5.0.5 Conclusions and Recommendations

Overall, utilizing a QIS for reading nitrogen vacancy centers in quantum sensing applications has the potential to enhance sensitivity, resolution, and dynamic range. Additionally, it could result in faster read out times and lower power consumption compared to CMOS image sensors. However, the QIS technology is still emerging, and further research and development is necessary to fully realize its potential in quantum sensing applications.

In conclusion, the detailed comparative analysis suggests that the QIS sensor is more suitable for NV center quantum sensing based on the provided data and requirements. However, these conclusions are based solely on the provided data and do not take into account practical factors such as cost. Further investigation and practical considerations are necessary before making a definitive statement.

Bonus further analysis: an external interview

In Misonou et al. [10], the research team used a Basler-based CCD camera for NV center read out. This decision was based on the group's prior experience with the device [10]. The Basler ace camera, often referred to as a "workhorse camera," is a cost-effective, versatile, high-definition option that can operate at speeds of up to 3 kHz while maintaining a reduced ROI. This image sensor performs well under adequate lighting conditions and was coupled with the quantum diamond microscope for read out [9]. In the summer of 2021, I had the opportunity to speak directly with Matthew Turner, the second author of the aforementioned paper. If the QIS were used instead of the Basler ace camera, there would be no need to integrate the quantum diamond microscope.

The QIS vs. CMOS Analysis

Furthermore, we discussed how the QIS would also be great for scaling the number of photons or qubits that can be read at once, compared to SPADs. Since photon counting data has not been available historically, it is unclear how this knowledge could benefit scientists. However, that does not mean that the applications and benefits do not exist. The QIS will have a significant impact on experiments involving low-density samples, low-light systems, noise-sensitive systems, and systems where precise photon counting is crucial. The QIS is worth researching in comparison to current industry technology, especially for the specific applications in which the QIS would excel.

| | QIS | Excelitas SPCM-AQRH-16-FC |
|--------------------|---------------------------|-----------------------------|
| FPS | 30-1000 | 164 |
| Sensor Size | 4.5 mm x 4.5 mm | 11.3 mm x 7.1 mm |
| Resolution (H x V) | 1024 px x 1024 px | 1920 px x 1200 px |
| Pixel size (H x V) | 1.1 μ m x 1.1 μ m | 5.86 μ m x 5.86 μ m |
| Quantum Efficiency | 76% @520 nm | 70% @650 nm |
| Dynamic range | 80 dB | 35 Mcps |
| Power req | 600 mW | 3.4 W |
| Read Noise | 0.019 e- rms | 6.6 e- |
| Dark current | 0.009 e-/sec/pix @ RT | |

- Single-photon sensitivity:** The QIS's ability to detect single photons enables the sensor to capture weak signals from NV centers with high precision. This single-photon sensitivity allows for better signal-to-noise ratios, making the QIS more suitable for detecting subtle changes in the NV center's fluorescence in response to external stimuli.
- High spatial resolution:** Due to the small size and high density of pixels, a QIS provides higher spatial resolution compared to traditional CMOS sensors. This could enable more accurate mapping of the local environment

The QIS vs. CMOS Analysis

surrounding NV centers and enhance the spatial resolution of quantum sensing measurements.

3. **High dynamic range:** The QIS's high dynamic range allows it to capture a wide range of light intensities, enabling it to resolve both bright and dim signals from NV centers. This can be especially advantageous when measuring signals that exhibit significant variations in intensity, such as when detecting magnetic or electric fields with substantial spatial gradients.
4. **High frame rate:** QIS technology enables high frame rates, potentially reaching thousands of frames per second. This can be advantageous when monitoring fast-changing physical quantities or observing dynamic processes that involve NV centers, such as relaxation and coherence times in quantum systems.
5. **Low power consumption:** QIS sensors consume less power than traditional CMOS image sensors, which can be crucial when integrating quantum sensors into portable or battery-powered devices.

Chapter 6

Conclusion

6.1 Future Research

This thesis focused on the construction of a setup to allow for quantum control of NV ensembles. NV ensemble manipulation requires less optical, green laser precision. The number of photons (and thus fluorescence) is also increased, enabling easier detection of changes [10]. Given that the photodiode was already utilizing converging lens and a 13 dB amplifier, the illumination of an NV ensemble rather than a single NV center was crucial. For the purpose of quantum sensing, control of an NV center ensemble may be preferred.

However, if NV centers are going to continued to be explored as qubits, it is imperative to obtain single spin read outs. The photodiode can not detect single centers, only ensembles. The state of the art for single spin detection is typically a SPAD (Single Photon Avalanche Diode), but notoriously these devices can not collect ensemble data. Since the QIS has a much greater sensitivity (even without a converging lens or amplifier) and smaller chip size, the Quanta Image Sensor seems

6.2 Closing Remarks

to be perfect as a NV center qubit read out, particularly for coupled qubits.

In order to measure if one or more NV centers are being read out is to conduct an experimental protocol called the G2 measurement experiment (also known as the R correlation measurement). Via an optical detector, the likelihood of a photon τ seconds after a photon measured at time t can be determined via an auto-correlation function: $G(\tau) = \langle g(t), g(t + \tau) \rangle$. Photons of an NV center can only be emitted approximately every 1 microsecond. Thus, if no photons are observed at $\tau < 1 \mu\text{s}$, there must be more than one NV center. In the upcoming weeks, I hope to utilize a new diamond sample to begin to detect single NV centers.

6.2 Closing Remarks

In conclusion, this senior thesis has provided a comprehensive investigation of the properties and behavior of nitrogen-vacancy centers in diamond through a series of experiments, including CW ODMR, pulsed ODMR, T_1 decay, Rabi oscillation, and Hahn Echo. These experiments have contributed to a deeper understanding of the underlying physics governing NV centers.

Appendix

In this appendix, I have included the code I used for my analysis.

6.3 Setup procedures

6.3.1 Version 3 - pulsed ODMR, Rabi oscillations, and Hahn Echo

1. Turn on the Hewlett Packard 8644B Synthesized Signal Generator (0.25-1030 MHz) and allow it to calibrate (6 min).
2. Turn on the Xantrex XPL 30-2D Dual DC power supply. Both voltages should be 5V, creating one 0-5V source and one -5V to 5V source.
3. Turn on the Traco power (24 Vdc; 6.25 A) power source for the LZY-22+ Minicircuits amplifier (0-24 V).
4. Windfreak SynthUSBII (34MHz – 4.4GHz) RF Signal Generator
5. Turn on the image sensor (see individual tutorials for Quanta Image Sensor and PDA36A2 Photodiode

6.4 Experiment Code

6. Turn on the amplifier for the photodiode amplifier, the Stanford research systems model SR560 low-noise pre-amplifier
7. Turn on the power source for the Spincore Pulseblaster DDS-I-300 board (12V, 0.37 A)
8. Set the Hewlett Packard 8644B Synthesized Signal Generator to 80 MHz and a power of -7.0 dB
9. Put on Laser Safety Goggles specced for 532 nm laser light and then turn on the G150-1803 532 nm Laser

6.3.2 Quanta Image Sensor Setup

6.3.3 CMOS Image Sensor (Photodiode) Setup

6.4 Experiment Code

6.4.1 CW ODMR experiment code

ODMR data extraction and plotting

```
% Katherine Lasonde
% CW ODMR graph creation for NV center

% Plot
filename = 'cw_odmr_data.xlsx';
```

6.4 Experiment Code

```
% Pull out the data
data = readtable(filename, 'VariableNamingRule', 'preserve
');

time_axis = (data.Frequency(2:end));
photon_num_axis = (data.Photons(2:end));
stnd_dev = (data.Deviation(2:end));

figure();
hold on;
grid;
plot(time_axis, photon_num_axis, 'b', LineWidth=3 );
errorbar(time_axis, photon_num_axis, stnd_dev, 'k');

hold off;
title("Microwave frequency (MHz) vs. Number of photons (CW
ODMR)");
xlabel('Microwave frequency (MHz)');
ylabel('Number of photons emitted by the NV center');
```

6.4.2 T_1 decay experiment code

Optical calibration

```
% Set internal clock frequency (MHz)
CLOCK_FREQ = 300
```

6.4 Experiment Code

```
% define output addresses
laser_on_only = 0b1001;
microwave_on_only = 0b0010;
both_off = 0x00;

% Adds path to the folder that contains all PulseBlaster
functions

% This folder is located in the PulseBlaster MATLAB GUI
package

addpath('C:\Matlab experiment code\PulseBlasterMatGUI_2017
-0111_64\Matlab_SpinAPI\');
addpath('C:\Users\Top Spin\Desktop\cleveland-qis\');

% Selects first PulseBlaster
pb_select_board(0);

% Initializes PulseBlaster
pb_init();

% Set Clock Frequency (MHz) to 100 MHz
pb_core_clock(CLOCK_FREQ);

% Start programming
```

6.4 Experiment Code

```
pb_start_programming('PULSE_PROGRAM');

pb_inst_pbonly(both_off, 0,0, 5*us_second);
pb_inst_pbonly(0,6,0,5*us_second);

% Close communication with PulseBlaster

pb_stop_programming();
pb_stop();
pb_start();
pb_close();

% Unload the library

unloadlibrary('spinapi64');
```

T₁ decay data collection

```
% Katherine Lasonde
% February 2023
% A program to run the T1 experimental protocol

global SPINAPI_DLL_NAME
SPINAPI_DLL_NAME = 'spinapi64';

function t1_measurement_cleveland_qis(t_delay, num_trials)

    % Set internal clock frequency (MHz)
```

6.4 Experiment Code

```
CLOCK_FREQ = 0.001;

us_second = 100000000; % define a microsecond

% Adds path to the folder that contains all
% PulseBlaster functions

% This folder is located in the PulseBlaster MATLAB
% GUI package

addpath('C:\Matlab experiment code\
PulseBlasterMatGUI_2017-0111_64\Matlab_SpinAPI\');

addpath('C:\Users\Top Spin\Desktop\cleveland-qis\');

% Loads spinapi64 library and both headers: spinapi.h
% and pulseblaster.h

if ~libisloaded('spinapi64')
    % All files are located in SpinAPI folder
    loadlibrary('C:\SpinCore\SpinAPI\lib\spinapi64.dll
    ', ...
    'C:\SpinCore\SpinAPI\include\spinapi.h
    ', 'addheader',...
    'C:\SpinCore\SpinAPI\include\
    pulseblaster.h');

end

% Selects first PulseBlaster
```

6.4 Experiment Code

```
pb_select_board(0);

% Initializes PulseBlaster
pb_init();

% Set Clock Frequency (MHz) to 100 MHz
pb_core_clock(CLOCK_FREQ);

% Retrieve firmware ID and prints in Command Window
firm_id = pb_get_firmware_id();
dev_id = bitshift(bitand(firm_id,hex2dec('FF00')), -8);
rev_id = bitand(firm_id,hex2dec('00FF'));
firmware_ID = sprintf('%d - %d', dev_id, rev_id)

% Start programming
pb_start_programming('PULSE_PROGRAM');

% Take the number of samples needed
for n=1:1:num_trials
    % First, a 15 us pulse
    pb_inst_pbonly(16777215, 0, 0, 15*us_second);

    % Second, turn off for a variable delay
    pb_inst_pbonly(0, 0, 0, t_delay*us_second);
```

6.4 Experiment Code

```
% Trigger the QIS to take in signal  
  
% Call the python script to capture a single frame  
pyrunfile('C:\Users\Top Spin\Desktop\cleveland-qis  
\\kat_matlab_rabi.py');  
  
% Third, turn on for 3 us  
pb_inst_pbonly(16777215,0,0,3*us_second);  
  
% Finally, turn off for 5 ms and then branch back  
to instruction 0  
pb_inst_pbonly(0,6,0,3000*us_second);  
end  
  
% Close communication with PulseBlaster  
pb_stop_programming();  
pb_stop();  
pb_start();  
pb_close();  
  
% Unload the library  
unloadlibrary('spinapi64');  
end
```

6.4 Experiment Code

```
% Start to run the testing
addpath('C:\Users\Top Spin\Desktop\cleveland-qis\kat_data'
);

% Create excel file
headers = {'Time', 'Photons', 'StandardDeviation'}
filename = 't1_qis_data.xlsx';
writecell(headers, filename);

% Define the number of trials
num_trials = 3;

% Start at t_delay = 100 us and increment every 100 us
% until at 5000 us
for t_delay = 100:100:4000
    % Collect the data
    t1_measurement_cleveland_qis(t_delay, num_trials);

    % Collect the average number
    [ave_num_photons, standard_deviation] =
        t1_qis_analysis(t_delay);
    writematrix([t_delay, ave_num_photons,
        standard_deviation], filename, 'WriteMode', 'append')
;
```

6.4 Experiment Code

```
end
```

T₁ decay data extraction and plotting

```
% T1 grapher for NV center
v = load('t1_curve.sfit', '-mat');
my_model = v.savedSession.AllFitdevsAndConfigs{2, 1}.

    Fitdev.Fit

% Plot
filename = 't1_qis_data_real.xlsx';
% Pull out the data
data = readtable(filename, 'VariableNamingRule', 'preserve
');
time_axis = (data.Var1(2:end));
photon_num_axis = (data.Var2(2:end));
stnd_dev = (data.Var3(2:end));

figure();
hold on;
grid;
scatter(time_axis, photon_num_axis);
errorbar(time_axis, photon_num_axis, stnd_dev, 'k');
h = plot(my_model, 'r');
h.LineWidth = 2;
```

6.4 Experiment Code

```
legend('Raw data points', 'Error bars', 'Line of best fit:  
y=a*exp(-x/b)+c')  
  
hold off;  
  
title("Time delay (ns) vs. Number of photons in T1 decay  
protocol");  
  
xlabel('Time delay (ns)');  
ylabel('Number of photons emitted by the NV center');
```

6.4.3 Pulsed ODMR experiment code

Pulsed ODMR data collection

```
%% Pulsed ODMR MATLAB code  
  
% Set internal clock frequency (MHz)  
CLOCK_FREQ = 0.001;  
  
% define a microsecond  
us_second = 100000000;  
  
% define output addresses  
laser_on_only = 0b0010;  
microwave_on_only = 0b0001;  
both_off = 0x00;
```

6.4 Experiment Code

```
% Selects first PulseBlaster
pb_select_board(0);

% Initializes PulseBlaster
pb_init();

% Set Clock Frequency (MHz) to 100 MHz
pb_core_clock(CLOCK_FREQ);

% Start programming
pb_start_programming('PULSE_PROGRAM');

% First, turn the laser on for 5 us
pb_inst_pbonly(laser_on_only, 0, 0, 5*us_second);

% Second, turn off everything for 500 us
pb_inst_pbonly(both_off, 0, 0, 5*us_second);

% Third, turn on microwave for 5 us
pb_inst_pbonly(microwave_on_only, 0, 0, 5*us_second);

% Fourth, turn off both for t_padding = 2 us
pb_inst_pbonly(both_off, 0, 0, 2*us_second);
```

6.4 Experiment Code

```
% Fifth, turn on the laser for 5 us to readout  
pb_inst_pbonly(laser_on_only, 0, 0, 5*us_second);  
  
% Finally, turn off both and for 1000 us and reset  
pb_inst_pbonly(0,6,0,1000*us_second);
```

Pulsed ODMR data extraction and plotting

```
% Katherine Lasonde  
% Pulsed ODMR for NV center  
  
filename = 'lasonde_pulsed_odmr_real.xlsx';  
  
% Pull out the data  
data = readtable(filename, 'VariableNamingRule', 'preserve'  
');  
time_axis = (data.Time(2:end));  
photon_num_axis = (data.Photons(2:end));  
stnd_dev = (data.Deviation(2:end));  
  
figure();  
hold on;  
grid;  
scatter(time_axis, photon_num_axis);  
plot(time_axis, smooth(photon_num_axis), 'k--', "LineWidth
```

6.4 Experiment Code

```
" , 0.8) ;  
errorbar(time_axis, photon_num_axis, stnd_dev, 'r', "  
LineWidth", 0.8);  
legend('Raw data points', 'Average fit line', 'Error bars  
' )  
  
hold off;  
title("Time delay (ns) vs. Number of photons in Pulsed  
ODMR protocol");  
xlabel('Time delay (ns)') ;  
ylabel('Number of photons emitted by the NV center');
```

6.4.4 Rabi oscillation experiment code

Rabi oscillation data collection

```
% Start programming  
pb_start_programming('PULSE_PROGRAM');  
  
for t_delay=0.05:0.05:3  
    % First, turn the laser on for 5 us  
    pb_inst_pbonly(laser_on_only, 0, 0, 5*us_second);  
  
    % Second, turn off everything for 500 us  
    pb_inst_pbonly(both_off, 0, 0, 5*us_second);
```

6.4 Experiment Code

```
% Third, turn on microwave for 5 us
pb_inst_pbonly(microwave_on_only,0,0,t_delay*us_second
);

% Trigger the QIS to take in signal

% % Call the python script to capture a single frame
% pyrunfile('C:\Users\Top Spin\Desktop\cleveland-qis\
kat_matlab.py');

% Fourth, turn off both for t_padding = 2 us
pb_inst_pbonly(both_off, 0, 0, 1*us_second);

% Call the python script to capture a single frame
pyrunfile('C:\Users\Top Spin\Desktop\cleveland-qis\
kat_matlab.py');

pb_inst_pbonly(both_off, 0, 0, 1*us_second);

% Fifth, turn on the laser for 5 us to readout
pb_inst_pbonly(laser_on_only, 0, 0, 5*us_second);

% Finally, turn off both and for 1000 us and reset
pb_inst_pbonly(0,0,0,1000*us_second);
```

6.4 Experiment Code

```
end

pb_inst_pbonly(0,0,0,1000*us_second);
```

Rabi oscillation data extraction and plotting

```
v = load('t2_curve.sfit', '-mat');
my_model = v.savedSession.AllFitdevsAndConfigs{1, 1}.  
Fitdev.Fit

%% Taking the excel file, create a graph
% a = xlsread('rabi_data_final.xlsx');
% save rabi.mat a;

% Plot
filename = 'han_echo_data_4.xlsx'; %'rabi_data.xlsx';

% Pull out the data
data = readtable(filename, 'VariableNamingRule', 'preserve  

```

6.4 Experiment Code

```
grid;

scatter(time_axis, photon_num_axis, 'kx');

plot(time_axis, smooth(photon_num_axis), 'b');

h = plot(my_model, 'r');

h.LineWidth = 2;

legend('Raw data points', 'Fitted average', 'Line of best

fit: y=a*exp(-x/b)+c')

hold off;

title("Time delay (ns) vs. Number of photons emitted

during Han Echo experiment");

xlabel('Time delay (nanoseconds)') ;

ylabel('Number of photons emitted by the NV center');
```

6.4.5 Hahn Echo (T_2) experiment code

Hahn Echo (T_2) data collection

```
% Start programming

pb_start_programming('PULSE_PROGRAM');

PI_pulse_length = 0.7968; %ns

half_pi_pulse_length = PI_pulse_length/2;

%

for t_delay=0.1:0.1:10
```

6.4 Experiment Code

```
% First, turn the laser on for 5 us
pb_inst_pbonly(laser_on_only, 0, 0, 5*us_second);

% Second, turn off everything for 500 us
pb_inst_pbonly(both_off, 0,0, 2*us_second);

% Third, turn on microwave for 5 us
pb_inst_pbonly(microwave_on_only,0,0,
                half_pi_pulse_length*us_second);
pb_inst_pbonly(both_off, 0,0, t_delay*us_second);

pb_inst_pbonly(microwave_on_only,0,0,PI_pulse_length*
                us_second);
pb_inst_pbonly(both_off, 0,0, t_delay*us_second);

pb_inst_pbonly(microwave_on_only,0,0,
                half_pi_pulse_length*us_second);

% Trigger the QIS to take in signal
% Fourth, turn off both for t_padding = 2 us
pb_inst_pbonly(both_off, 0, 0, 1*us_second);

% Call the python script to capture a single frame
pyrunfile('C:\Users\Top Spin\Desktop\cleveland-qis\
```

6.4 Experiment Code

```
kat_matlab.py');

pb_inst_pbonly(both_off, 0, 0, 1*us_second);

% Fifth, turn on the laser for 5 us to readout
pb_inst_pbonly(laser_on_only, 0, 0, 5*us_second);

% Finally, turn off both and for 1000 us and reset
pb_inst_pbonly(0,0,0,1000*us_second);

end

pb_inst_pbonly(0,0,0,1000*us_second);
```

6.4.6 QIS data collection

```
import sensor_control_utilities as scu
import data_process_utilities as dpu
import scipy.io
import numpy as np
import ok
import datetime
import os
from time import sleep
import datetime
from sensor_program import EN_PGA, CMS_NUM
```

6.4 Experiment Code

```
# Sets how many frames are collected in one readout
nframe = 1

# Set to the num of samples used to average CMS samples
CMS = CMS_NUM

# PGA Settings
PGA_EN = int(EN_PGA)
ROW_INT_TIME = 0
# Programs sensor integration time
scu.set_int_time(dev, ROW_INT_TIME)

# file name for directory
testing_dir = "./kat_data"# + "./" + t_delay + "/"

# Collect raw data from sensor
buf_a0 = scu.data_pipein_frame(dev, nframe)

# Translate raw data into integer data
out = dpu.dt_process_bin(buf_a0)/CMS

# Re-map integer data into final image. For third input,
# set to 1 when EN_PGA = '1' otherwise set to 0
```

6.5 List of parts

```
img, rst, tx = dpu.map_img_multi(out, nframe, PGA_EN)

current_time = datetime.datetime.now().strftime('%Y-%m-%d
        -%I-%M-%S-%p')

# file name variable

fileName = testing_dir + "/capture_section_" + str(
    current_time)

# Save data as .mat file

scipy.io.savemat(fileName, {"img": img}, do_compression=
    True)

# get code start time for file name

end_time = datetime.datetime.now()

print("Finished at: " + str(end_time))
```

6.5 List of parts

6.5.1 Optical components

1. SpinCore PulseBlasterDDS-300
2. Thorlabs Natural density (ND) filter
3. Thorlabs Dichroic filter
4. Thorlabs Mirror

6.5 List of parts

5. Thorlabs N-BK7 Plano-Convex Lens, $\varnothing 1/2"$, f = 20 mm, AR Coating: 350 - 700 nm
6. Thorlabs N-BK7 Plano-Convex Lens, $\varnothing 1"$, f = 100 mm, AR Coating: 350 - 700 nm
7. Thorlabs Adapter with External SM1 Threads and Internal SM05 Threads, 0.15" Long
8. Thorlabs SM05 Lens Tube, 0.30" Thread Depth, One Retaining Ring Included
9. Thorlabs 30 mm Cage Cube Precision Kinematic Rotation Platform
10. Thorlabs Externally SM1-Threaded End Cap
11. Thorlabs Blank Cover Plate
12. Thorlabs $\varnothing 1"$ Optic Mount for 30 mm Cage Cube with Setscrew Optic Retention
13. Thorlabs $\varnothing 1.5"$ Slip-On Post Clamp, Imperial
14. Thorlabs N-BK7 Plano-Convex Lens, $\varnothing 1"$, f = 60 mm, AR Coating: 400 - 1100 nm
15. Thorlabs 10X Olympus Plan Achromat Objective, 0.25 NA, 10.6 mm WD
16. Thorlabs RMS-Threaded 30 mm Cage Plate, 0.35" Thick, 8-32 Tap
17. Thorlabs N-BK7 Bi-Convex Lens, $\varnothing 1"$, f = 100.0 mm, Uncoated
18. Thorlabs SM1 Lens Tube Spacer, 1" Long

6.5 List of parts

19. Thorlabs Right-Angle Kinematic Mirror Mount with Smooth Cage Rod Bores, 30 mm Cage System and SM1 Compatible, 8-32 and 1/4"-20 Mounting Holes
20. Thorlabs Slim Right-Angle Bracket with Counterbored ; 1/4"-20 Tapped Holes
21. Thorlabs Single Axis Translation Stage, 2" Travel
22. Thorlabs LT Series Angle Bracket
23. Thorlabs Kinesis® 30 mm Motorized XY Translation Stage, 1/4"-20 Tapped Holes
24. Thorlabs Compact Rotation Stage with Fine Adjustment, 8-32 and 4-40 Taps
25. Thorlabs Mounting Bracket for Ø1" Posts, 8 (M4) Counterbores and Slot
26. Thorlabs Dovetail Optical Rail, 6", Imperial
27. Thorlabs Adjustable Flip Platform, 8-32 Taps
28. Thorlabs Ø1.5" Mounting Post, 1/4"-20 Taps, L = 8"
29. Thorlabs Ø1" Pedestal Pillar Post, 8-32 Taps, L = 6"
30. Thorlabs LRM1 1" optical holders
31. Thorlabs RS1P8E 1" pedestal posts
32. Thorlabs RS0.5P8E 0.5" pedestal post
33. Thorlabs CF125C clamping forks
34. Thorlabs TRF90 flip mount

6.5 List of parts

35. Thorlabs TR2F90 90° Flip Mount
36. Thorlabs PF20-03-G01 Ø2" Protected Aluminum mirror

Bibliography

- [1] Simeon Bogdanov, Mikhail Y. Shalaginov, Alexei Lagutchev, Chin-Cheng Chi-ang, Deesha Shah, Alexander S. Baburin, Ilya A. Ryzhikov, Ilya A. Rodionov, Alexandra Boltasseva, and Vladimir M. Shalaev. Ultrabright room-temperature single-photon emission from nanodiamond nitrogen-vacancy centers with sub-nanosecond excited-state lifetime. 2017.
- [2] Eric R. Fossum, Jiaju Ma, Saleh Masoodian, Leo Anzagira, and Rachel Zizza. The quanta image sensor: Every photon counts. *Sensors*, 16(8), 2016.
- [3] K.-M. C. Fu, C. Santori, P. E. Barclay, and R. G. Beausoleil. Conversion of neutral nitrogen-vacancy centers to negatively charged nitrogen-vacancy centers through selective oxidation. *Applied Physics Letters*, 96(12):121907, March 2010. Publisher: American Institute of Physics.
- [4] Lars G. Hanson. Is quantum mechanics necessary for understanding magnetic resonance? *Concepts in Magnetic Resonance Part A*, 32A(5):329–340, 2008.
- [5] Ariful Haque and Sharaf Sumaiya. An overview on the formation and processing of nitrogen-vacancy photonic centers in diamond by ion implantation. *Journal of Manufacturing and Materials Processing*, 1(1), 2017.

BIBLIOGRAPHY

- [6] Jaroslav Hruby, Michal Gulka, Massimo Mongillo, Iuliana P. Radu, Michael V. Petrov, Emilie Bourgeois, and Milos Nesladek. Magnetic field sensitivity of the photoelectrically read nitrogen-vacancy centers in diamond. *Applied Physics Letters*, 120(16), 04 2022. 162402.
- [7] Fedor Jelezko, Bernhard Grotz, and Liam Mcguinness. Nitrogen-vacancy centers close to surfaces. *MRS Bulletin*, 38, 02 2013.
- [8] Andrii Lazariev, Silvia Arroyo-Camejo, Ganesh Rahane, Vinaya Kumar Kavata-mane, and Gopalakrishnan Balasubramanian. Dynamical sensitivity control of a single-spin quantum sensor, 2015.
- [9] Edlyn V. Levine, Matthew J. Turner, Pauli Kehayias, Connor A. Hart, Nicholas Langellier, Raisa Trubko, David R. Glenn, Roger R. Fu, and Ronald L. Walsworth. Principles and techniques of the quantum diamond microscope. *Nanophotonics*, 8(11):1945–1973, 2019.
- [10] Daiki Misonou, Kento Sasaki, Shuntaro Ishizu, Yasuaki Monnai, Kohei M. Itoh, and Eisuke Abe. Construction and operation of a tabletop system for nanoscale magnetometry with single nitrogen-vacancy centers in diamond. *AIP Advances*, 10(2):025206, February 2020. arXiv: 2002.02113.
- [11] M. Mrozek, D. Rudnicki, P. Kehayias, A. Jarmola, D. Budker, and W. Gawlik. Longitudinal spin relaxation in nitrogen-vacancy ensembles in diamond, May 2015. arXiv:1505.02253 [cond-mat, physics:physics].
- [12] B. A. Myers, A. Das, M. C. Dartailh, K. Ohno, D. D. Awschalom, and A.

BIBLIOGRAPHY

- C. Bleszynski Jayich. Probing surface noise with depth-calibrated spins in diamond. *Physical Review Letters*, 113(2), jul 2014.
- [13] Aldona Mzyk, Alina Sigaeva, and Romana Schirhagl. Relaxometry with nitrogen vacancy (nv) centers in diamond. *Accounts of Chemical Research*, 55(24):3572–3580, 2022. PMID: 36475573.
- [14] NXP Semiconductors. *High-speed CAN transceiver*, 4 2013. Rev. 3.
- [15] Huijin Park, Junghyun Lee, Sangwook Han, Sangwon Oh, and Hosung Seo. De-coherence of nitrogen-vacancy spin ensembles in a nitrogen electron-nuclear spin bath in diamond. *npj Quantum Information*, 8(1):1–6, August 2022. Number: 1 Publisher: Nature Publishing Group.
- [16] Iona Popa. Pulsed magnetic resonance on single defect centers in diamond. 2006.
- [17] Phila Rembold, Nimba Oshnik, Matthias M. Müller, Simone Montangero, Tommaso Calarco, and Elke Neu. Introduction to quantum optimal control for quantum sensing with nitrogen-vacancy centers in diamond. *AVS Quantum Science*, 2(2):024701, June 2020. Publisher: American Vacuum Society.
- [18] T. Rosskopf, A. Dussaux, K. Ohashi, M. Loretz, R. Schirhagl, H. Watanabe, S. Shikata, K. M. Itoh, and C. L. Degen. Investigation of surface magnetic noise by shallow spins in diamond. *Physical Review Letters*, 112(14), apr 2014.
- [19] Vikas K. Sewani, Hyma H. Vallabhapurapu, Yang Yang, Hannes R. Firgau, Chris Adambukulam, Brett C. Johnson, Jarryd J. Pla, and Arne Laucht. Coherent control of NV centers in diamond in a quantum teaching lab. *American Journal of Physics*, 88(12):1156–1169, December 2020.

BIBLIOGRAPHY

- [20] Xuerui Song, Guanzhong Wang, Xiaodi Liu, Fupan Feng, Junfeng Wang, Liren Lou, and Wei Zhu. Generation of nitrogen-vacancy color center in nanodiamonds by high temperature annealing. *Applied Physics Letters*, 102(13), 04 2013. 133109.
- [21] Xuerui Song, Jian Zhang, Fupan Feng, Junfeng Wang, Wenlong Zhang, Liren Lou, Wei Zhu, and Guanzhong Wang. A statistical correlation investigation for the role of surface spins to the spin relaxation of nitrogen vacancy centers. *AIP Advances*, 4(4):047103, April 2014.
- [22] Kseniia Volkova, Julia Heupel, Sergei Trofimov, Fridtjof Betz, Rémi Colom, Rowan W. MacQueen, Sapida Akhundzada, Meike Reginka, Arno Ehresmann, Johann Peter Reithmaier, Sven Burger, Cyril Popov, and Boris Naydenov. Optical and Spin Properties of NV Center Ensembles in Diamond Nano-Pillars. *Nanomaterials*, 12(9):1516, April 2022.
- [23] Haimei Zhang, Carina Belvin, Wanyi Li, Jennifer Wang, Julia Wainwright, Robbie Berg, and Joshua Bridger. Little bits of diamond: Optically detected magnetic resonance of nitrogen-vacancy centers. *American Journal of Physics*, 86(3):225–236, March 2018. arXiv: 1708.00418.